

# Development of an optical sensor system for the characterization of Cascadia Basin, Canada

Andreas Gärtner

---

Masters thesis  
11. December 2018

First Examiner: Prof. Dr. Elisa Resconi  
Second Examiner: Prof. Dr. Laura Fabbietti

**Technical University of Munich**  
Department of Physics  
Experimental Physics with Cosmic Particles





# Abstract

High energy neutrino astronomy uses large volume detectors to search for astrophysical neutrinos sources. Detectors such as IceCube at the Geographic South Pole instrumented a cubic kilometer of ice measuring Cherenkov radiation created by neutrino-matter interactions. Using the clear water of the deep sea as the Cherenkov medium has so far posed severe difficulties in deploying and maintaining the offshore infrastructure, although a detector of this type is currently developed by KM3NeT in the Mediterranean.

Ocean Networks Canada (ONC), an initiative of the University of Victoria, has been creating and maintaining the longest deep sea infrastructure available for scientific instruments, located off the coast of Canada. One of their network nodes, located on the Pacific abyssal plain of Cascadia Basin, could be in an ideal position for a future neutrino telescope.

This thesis concerns the Strings for Absorption Length in Water (STRAW), which have been developed in 2018 in collaboration with ONC and the University of Alberta. Two strings with optical modules have been deployed at Cascadia Basin in order to measure the optical properties of the water and study the feasibility of a larger setup. The primary measurement goals are absorption, scattering and background radiation.

In this thesis I will report about the mechanical setup of the two strings and the details of the deployment mechanism and operation.



# Contents

<b>Introduction</b>	<b>6</b>
<b>1 Neutrino physics and large volume detectors</b>	<b>8</b>
1.1 Postulation and discovery . . . . .	8
1.2 Sources . . . . .	10
1.3 Neutrino telescopes . . . . .	11
1.4 Relevant environment parameters for neutrino telescopes . . . . .	13
<b>2 Ocean Networks Canada</b>	<b>15</b>
2.1 Overview . . . . .	15
2.2 Infrastructure and instrument platforms . . . . .	15
2.3 Deployment method . . . . .	17
2.4 Remotely Operated Platform for Ocean Science (ROPOS) . . . . .	17
<b>3 Simulations and expected environment</b>	<b>20</b>
3.1 Water transmittivity . . . . .	20
3.2 The string in the current . . . . .	21
3.3 Preliminary light simulation . . . . .	21
<b>4 The double string</b>	<b>25</b>
<b>5 Modules</b>	<b>27</b>
5.1 POCAM . . . . .	27
5.1.1 Housing . . . . .	27
5.1.2 Integrating sphere . . . . .	27
5.1.3 In-situ calibration . . . . .	28
5.1.4 Electronics . . . . .	28
5.1.5 Kapustinsky circuit . . . . .	29
5.2 SDOM . . . . .	30
5.2.1 Housing . . . . .	30
5.2.2 Photomultiplier . . . . .	30
5.2.3 Electronics . . . . .	31
5.3 The Medusa board . . . . .	31
<b>6 Material choice and corrosion protection</b>	<b>34</b>
6.1 Materials overview . . . . .	34
6.2 Steel and steel protection . . . . .	34

6.3	Different metals in contact . . . . .	35
6.4	Zinc coating . . . . .	36
6.5	Paint . . . . .	37
6.6	Bolts and nuts . . . . .	37
6.7	Steel wires . . . . .	38
6.8	Overdesign . . . . .	38
6.9	Stainless steel corrosion . . . . .	38
6.10	Winch . . . . .	39
6.11	Choice of colors . . . . .	39
6.12	Non-metallic components . . . . .	40
<b>7</b>	<b>Construction</b>	<b>41</b>
7.1	Anchor . . . . .	41
7.2	Module mountings . . . . .	42
7.3	Spacers . . . . .	43
7.4	Top spacer . . . . .	45
7.5	Compensating anchor tilt . . . . .	46
7.6	Bottom spacer . . . . .	46
7.7	Mini junction box mounting . . . . .	47
7.8	Markings and nomenclature of strings and modules . . . . .	47
7.9	Steel wire rope . . . . .	48
7.10	Data cables . . . . .	49
7.11	Buoyancy . . . . .	50
7.12	Transport . . . . .	51
<b>8</b>	<b>Calibration and testing</b>	<b>53</b>
8.1	Measuring the data cable length . . . . .	53
8.2	Magnetometer . . . . .	53
8.3	Vibration testing . . . . .	55
8.4	Pressure testing . . . . .	56
<b>9</b>	<b>Designing a winch for string deployment</b>	<b>59</b>
9.1	Expected forces and dimensioning . . . . .	59
9.2	Material . . . . .	59
9.3	Motor . . . . .	60
9.4	Axle . . . . .	60
9.5	Wheel . . . . .	61
9.6	Frame . . . . .	62
9.7	String assembly and spooling . . . . .	62
<b>10</b>	<b>Deployment preparation and testing at Ocean Networks Canada</b>	<b>69</b>
<b>11</b>	<b>Deployment</b>	<b>73</b>

# List of abbreviations

ECP	Experimental Physics with Cosmic Particles, working group of the author at TUM
GVD	Gigaton Volume Detector, neutrino detector in Lake Baikal
ODI	Brand of underwater cables and connectors from Teledyne
ONC	Ocean Networks Canada, an initiative of the University of Victoria
PMT	Photomultiplier tube
POCAM	Precision Optical Calibration Module, a module creating isotropic nanosecond pulses
RIB	Rigid inflatable boat, a lightweight boat assisting the main vessel during deployment
POM	Polyoxymethylene, hard plastic
ROPOS	Remotely Operated Platform for Ocean Science, the ROV used during deployment
ROV	Remotely operated underwater vehicle, an unmanned submarine for inspection and maintenance of underwater structures
SDOM	STRAW Digital Optical Module
STRAW	Strings for Absorption Length in Water
TUM	Technical University of Munich
UVIC	University of Victoria
ZTL	Central Technology Lab of TUM

# Introduction

The Strings for Absorption Length in Water (STRAW) setup consists of two double strings placed at 37 m distance in Cascadia Basin.

Two types of optical instruments are mounted on the strings. The Precision Optical Calibration Module (POCAM), a calibration module developed for IceCube and already tested in GVD provides an isotropic light source creating nanosecond flashes of different wavelengths. The STRAW Digital Optical Module (SDOM) contains two photomultiplier tubes, one facing up and one facing down. Five SDOMs and three POCAMs compose STRAW. We study the absorption and scattering length measuring with the SDOMs the light emitted by POCAM flashes. When the POCAMs do not flash, the dark rate is measured, which is influenced by bioluminescence and radioactivity.

The goal of STRAW is not only to measure water properties, but to also to study the feasibility of a large neutrino telescope at Cascadia Basin with respect to infrastructure and deployment capabilities. We therefore chose a setup which mimics a larger detector as closely as possible, using optical modules and calibration light sources on mooring lines in the same way as they could be used in a future detector.

Each string has a buoyancy at the top and an anchor at the bottom. The strings have a length of 140 m in total with instruments at the heights of 30 m, 50 m, 70 m and 110 m. By using double strings we prevent the rotation of the modules around the strings, making sure that the modules of the two strings face each other. The strings were assembled at TUM, then spooled onto a newly developed winch, tested at ONC, and deployed in June 2018. Fig. 1 shows a sketch of the two STRAW strings. Four modules per string are connected to a mini junction box at the bottom, developed by ONC. The strings consist of two steel wire ropes each, which are kept apart by spacers. The strings are referred to as string Blue and string Yellow.

STRAW has started operation in summer 2018 and is currently taking continuous measurements. So far all modules are fully operational and the intactness of the strings has been checked twice by a remotely controlled underwater vehicle (ROV).

The instruments of STRAW will be described only briefly in this thesis, further information can be found in the complementary thesis by F. Henningsen [Hen18].

---

[Hen18] Felix Henningsen. "Optical Characterization of the Deep Pacific Ocean: Development of an Optical Sensor Array for a Future Neutrino Telescope". MA thesis. Technical University of Munich, July 2018

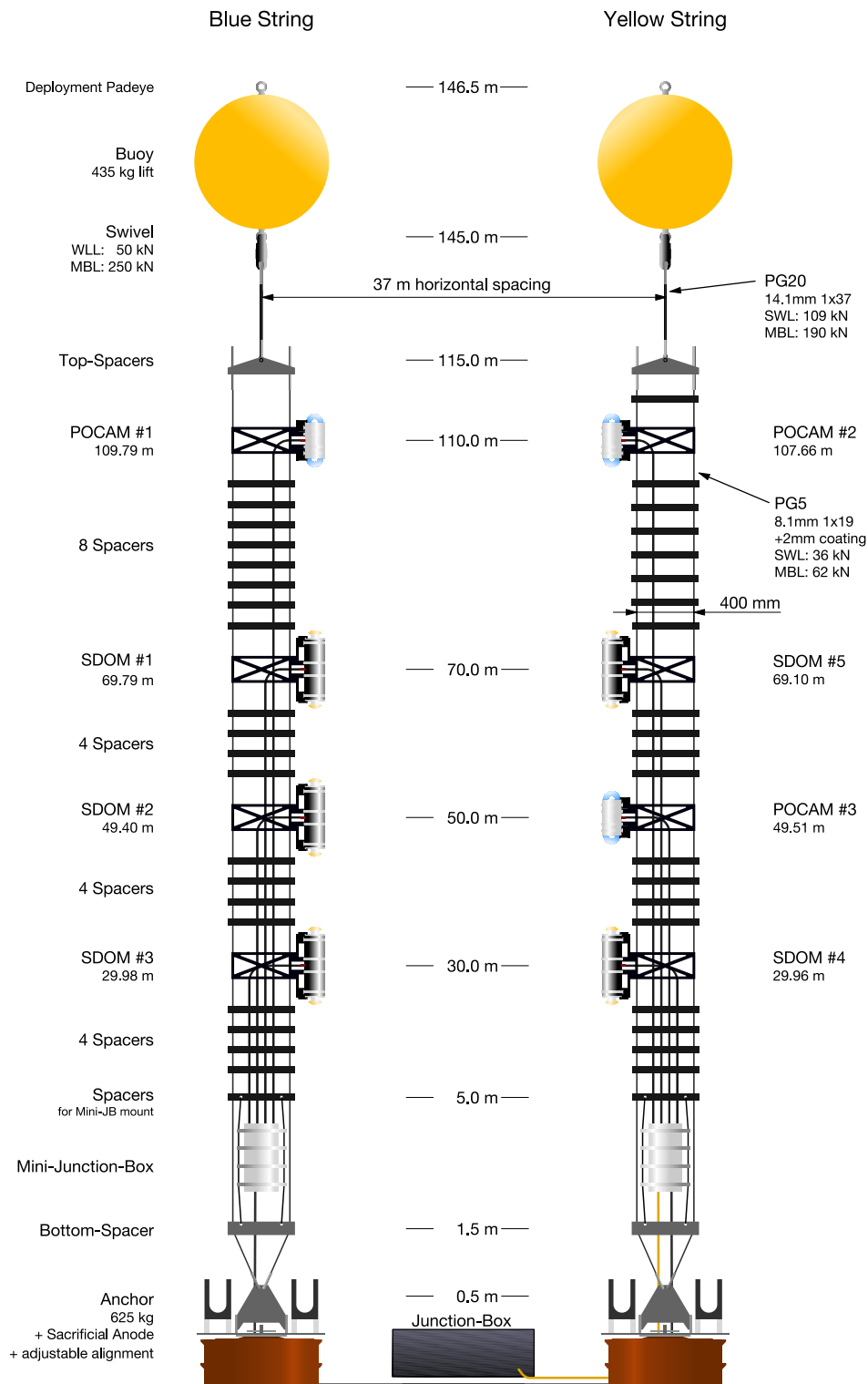


Figure 1: Overview of the two STRAW strings. Four modules per string are connected to a mini junction box at the bottom, developed by ONC. Each string consists of two steel lines, which are kept apart by spacers.

## Chapter 1

# Neutrino physics and large volume detectors

Neutrino astronomy is a relatively new field at the boundaries of particle physics and astronomy. It aims to detect neutrinos created in astrophysical sources using large neutrino telescopes, which extend up to one cubic kilometer in volume.

### 1.1 Postulation and discovery

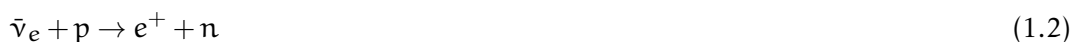
In 1930 Wolfgang Pauli suggested the existence of a light uncharged particle, a third product of the  $\beta$ -decay, to explain the continuous energy spectrum of the decay. Pauli suggested, that what was before considered a two-body decay (nucleus and electron), which should have a discrete spectrum, is in fact a three-body decay (nucleus, electron and neutrino), where the third particle had evaded detection.

Nowadays this particle, known as neutrino, is an integral part of the Standard Model of Particle Physics. Each charged lepton (electron, muon, and tauon) has a corresponding neutral neutrino partner. Neutrinos react only via the weak interaction, which is the weakest of the three forces in the Standard Model with cross sections of about  $10^{-44}$  cm. Unlike the other interactions, the weak interaction can not create bound states and is only relevant for flavor changes of particles, the most prominent example being the  $\beta$ -decay:



Just as the  $\beta$ -decay creates a (anti-)neutrino, the inverse  $\beta$ -decay can capture a neutrino and serve for neutrino detection. Due to the small cross section of the weak interaction, the probability for this process is negligible unless either a high neutrino flux or a high target volume is used.

The first detection of neutrinos was done in 1956 by Cowan and Reines [Cow+56] via the inverse  $\beta$ -decay



and consecutive reactions in water containing cadmium chloride. For this experiment, a layered setup of water tanks and scintillation detectors with photomultiplier tubes was

---

[Cow+56] C.L. Cowan et al. "Detection of the Free Neutrino: a Confirmation". In: *The Theory of Beta-Decay* (1956), pp. 129–135. doi: 10.1016/b978-0-08-006509-0.50008-9

placed in the strong anti-neutrino flux of a nuclear reactor, looking for the coincidence of the photons created by the positron annihilation and the neutron capture of the cadmium ions:

$$e^+ + e^- \rightarrow 2\gamma \quad (1.3)$$

$$n + {}^{113}\text{Cd}^{2+} \rightarrow {}^{114}\text{Cd}^{2+} + \gamma \quad (1.4)$$

Consecutively, muon neutrinos and tau neutrinos were discovered, where the experimentators made explicit use of the low interaction probability and therefore deep penetration of neutrinos through matter. In 1962, the first artificial neutrino beam was created to detect muon neutrinos [Dan+62]. A proton beam hitting a beryllium target produced fast pions. After a short free path, where the pions had time to partially decay into muons and muon neutrinos, a 14m steel shield filtered out everything except the neutrinos, which were detected in a 10t aluminium spark chamber.

In 2000, the DONUT collaboration detected the first tau neutrinos [Kod+01]. Similar to the muon neutrino detection, a proton beam hitting a tungsten target produced mesons, which in turn decayed into a multitude of secondary particles. Using a steel shield most non-neutrinos were filtered out. In a target consisting of many emulsion sheets the neutrinos would interact and create secondary particles, whose tracks left marks in the sheet. Using further detectors to identify secondary and tertiary particles, possible tau neutrino events were registered. Later, the emulsion layers were photographically developed and particle tracks were reconstructed. Four tau neutrino events were found, identifiably by a characteristic track of a tauon starting in the middle of the emulsion track, without any tracks leading up to it, and having a kink after few millimeters when the tauon decays.

These early experiments show a fundamental pattern of neutrino detection, the use of a detector with a large volume to compensate for low statistics, where the detector is placed after a shield filtering out most other particles.

The first neutrinos from an extraterrestrial source were discovered by the team of R. Davis Jr. [Cle+98]. Solar neutrinos are created during the proton fusion in the core of the sun:

$$p + p \rightarrow {}^2\text{H} + e^+ + \nu_e \quad (1.5)$$

In the Homestake Mine, 1.5km underground, a large tank filled with tetrachlorethylene was used as detection volume. Via the inverse beta decay  ${}^{37}\text{Cl}$  was transformed to radioactive  ${}^{37}\text{Ar}$ , which was flushed out regularly and collected. Then the decay of the  ${}^{37}\text{Ar}$  was measured. This experiment, being only sensitive to electron neutrinos, measured only a third of the expected solar neutrinos, starting the now famous solar neutrino problem.

Apart from astronomy, neutrinos play a significant role in modern particle physics research. The solar neutrino problem, for example, can be explained by the neutrinos having mass eigenstates different from their flavor eigenstates, which allows neutrinos to

[Dan+62] G. Danby et al. "Observation of high-energy neutrino reactions and the existence of two kinds of neutrinos". In: *10.1103/PhysRevLett.9.36* (1962). doi: 10.1103/PhysRevLett.9.36

[Kod+01] K. Kodama et al. "Observation of tau neutrino interactions". In: *Phys. Lett. B504* (2001), pp. 218–224. doi: 10.1016/S0370-2693(01)00307-0. arXiv: hep-ex/0012035 [hep-ex]

[Cle+98] B. T. Cleveland et al. "Measurement of the solar electron neutrino flux with the Homestake chlorine detector". In: *Astrophys. J.* 496 (1998), pp. 505–526. doi: 10.1086/305343

change their flavor during propagation (neutrino oscillation [McD05]). Different mass eigenstates require the neutrinos to have masses, however, the masses are exceptionally small and only upper limits could be measured so far ( $m_{\nu_e} < 2\text{eV}$  [PDG18]) and the mass hierarchy of the neutrinos is still unknown. In cosmology, neutrinos are used to explain the relative abundance of elements after the primordial nucleosynthesis and the anisotropies of the cosmic microwave background [Cyb+05].

## 1.2 Sources

Apart from artificially created neutrinos in reactors and accelerator beams, neutrinos come from various natural sources.

Solar neutrinos are created in the core of the sun. Unlike photons, which slowly diffuse through the dense sun matter and need several thousand years to leave the sun, neutrinos leave the sun undisturbed and allow a direct observation of the solar core [Bel+14]. Neutrinos created in other stars are usually too sparse to be measured with the exception of supernova neutrinos.

When a massive star collapses and explodes into a supernova, it does not only create a strong visible photon pulse, but also a strong neutrino pulse in the MeV-scale, which carries away most of the explosion energy [Jan17]. When in 1987 a star in the Large Magellanic Cloud turned into the supernova SN1987A, multiple neutrino detectors, including Kamiokande-II in Japan, detected a neutrino burst from the direction of SN1987A several hours before the optical detection of the supernova [Hir+87].

Atmospheric neutrinos are created by cosmic radiation hitting the atmosphere. The cosmic radiation, first discovered by Hess in 1912, consists of mainly protons and helium nuclei with energies stretching over ten orders of magnitude [Oli+14]. When hitting the atmosphere, secondary and tertiary particles, among them neutrinos, are created until the shower, covering many square kilometers, hits the ground. Large area detectors such as the Pierre-Auger-Observatory [Aab+15] and Telescope Array [Fuk15] were built to detect these showers. Atmospheric neutrinos are the dominant background in the search for astrophysical neutrinos. The IceCube neutrino detector, for example, uses the IceTop surface detector to detect showers and provide a veto against atmospheric muons and

[McD05] A. B. McDonald. “Evidence for neutrino oscillations. I. Solar and reactor neutrinos”. In: *Nucl. Phys.* A751 (2005), pp. 53–66. doi: 10.1016/j.nucphysa.2005.02.102. arXiv: nuc1-ex/0412005 [nuc1-ex]

[PDG18] M. Tanabashi et al. (Particle Data Group). “Review of Particle Physics”. In: *Phys. Rev. D* 98, 03001 (2018)

[Cyb+05] Richard H. Cyburt et al. “New BBN limits on physics beyond the standard model from  $^4\text{He}$ ”. In: *Astropart. Phys.* 23 (2005), pp. 313–323. doi: 10.1016/j.astropartphys.2005.01.005. arXiv: astro-ph/0408033 [astro-ph]

[Bel+14] G. Bellini et al. “Neutrinos from the primary proton–proton fusion process in the Sun”. In: *Nature* 512.7515 (2014), pp. 383–386. doi: 10.1038/nature13702

[Jan17] H. -Th. Janka. “Neutrino Emission from Supernovae”. In: (2017). doi: 10.1007/978-3-319-21846-5\_4. arXiv: 1702.08713 [astro-ph.HE]

[Hir+87] K. Hirata et al. “Observation of a Neutrino Burst from the Supernova SN 1987a”. In: *Phys. Rev. Lett.* 58 (1987). [727(1987)], pp. 1490–1493. doi: 10.1103/PhysRevLett.58.1490

[Oli+14] K. A. Olive et al. “Review of Particle Physics”. In: *Chin. Phys.* C38 (2014), p. 090001. doi: 10.1088/1674-1137/38/9/090001

[Aab+15] Alexander Aab et al. “The Pierre Auger Cosmic Ray Observatory”. In: *Nucl. Instrum. Meth.* A798 (2015), pp. 172–213. doi: 10.1016/j.nima.2015.06.058. arXiv: 1502.01323 [astro-ph.IM]

[Fuk15] Masaki Fukushima. “Recent Results from Telescope Array”. In: *EPJ Web Conf.* 99 (2015), p. 04004. doi: 10.1051/epjconf/20159904004. arXiv: 1503.06961 [astro-ph.HE]

neutrinos detected by IceCube in coincidence to the shower. [Abb+13].

Cosmogenic neutrinos are created when ultra high energy cosmic rays are scattered on the cosmic microwave background (Greisen-Sazepin-Kusmin-effect [ZK66]). These are the highest energy neutrinos and, as they propagate to earth without further deflection, are a unique tool for studying the universe on the PeV-scale [Aar+13].

At last, the cosmic neutrino background consists of neutrinos leftover from the neutrino decoupling shortly after the Big Bang. Massively redshifted, these neutrinos have energies below 1 meV and can not be detected directly by neutrino detectors. Nonetheless, as the decoupling of the neutrinos had a significant effect on the early universe, an indirect observation could be made based on the phase shift in the acoustic oscillations of the cosmic microwave background [Fol+15].

Fig. 1.1 shows the neutrino energy spectrum taken from [HK08].

### 1.3 Neutrino telescopes

The detection of astrophysical neutrinos faces the problem of extremely low predicted neutrino flux from astrophysical sources. Detectors compensate this by using detection volumes of up to one cubic kilometer.

The standard setup of a neutrino telescope is using a large volume of a transparent medium (ice or water). Neutrinos interact with the medium either via the neutral current, creating a hadronic shower

$$\nu_l + X \rightarrow \nu_l + Y \quad (1.6)$$

or via charged current, creating their charged lepton counterpart

$$\nu_l + X \rightarrow l + Y \quad (1.7)$$

In principle, the different interactions allow to distinguish between different neutrino flavors.

The charged lepton, carrying a part of the initial energy of the neutrino, creates Cherenkov radiation if it is faster than the speed of light in the medium. Optical modules consisting of photomultiplier tubes in pressure housings detect the created light. The energy and the direction of the neutrino can be reconstructed from the amount and the arrival times of the detected photons.

The three neutrino flavors show distinct patterns in the medium. Electron neutrinos, creating electrons, result in a short cascade, as the electron loses energy very quickly. The muon, being significantly heavier, forms a large linear track through the medium, often

---

[Abb+13] R. Abbasi et al. “IceTop: The surface component of IceCube”. In: *Nucl. Instrum. Meth.* A700 (2013), pp. 188–220. doi: 10.1016/j.nima.2012.10.067. arXiv: 1207.6326 [astro-ph.IM]

[ZK66] G. T. Zatsepin and V. A. Kusmin. “Upper limit of the spectrum of cosmic rays”. In: *JETP Lett.* 4 (1966). [*Pisma Zh. Eksp. Teor. Fiz.* 4,114(1966)], pp. 78–80

[Aar+13] M. G. Aartsen et al. “Probing the origin of cosmic rays with extremely high energy neutrinos using the IceCube Observatory”. In: *Phys. Rev. D* 88 (2013), p. 112008. doi: 10.1103/PhysRevD.88.112008. arXiv: 1310.5477 [astro-ph.HE]

[Fol+15] Brent Follin et al. “First Detection of the Acoustic Oscillation Phase Shift Expected from the Cosmic Neutrino Background”. In: *Phys. Rev. Lett.* 115.9 (2015), p. 091301. doi: 10.1103/PhysRevLett.115.091301. arXiv: 1503.07863 [astro-ph.CO]

[HK08] F. Halzen and S. R. Klein. “Astronomy and astrophysics with neutrinos”. In: *Physics Today* 61, 5, 29 (2008), pp. 29–35. doi: {10.1063/1.2930733}

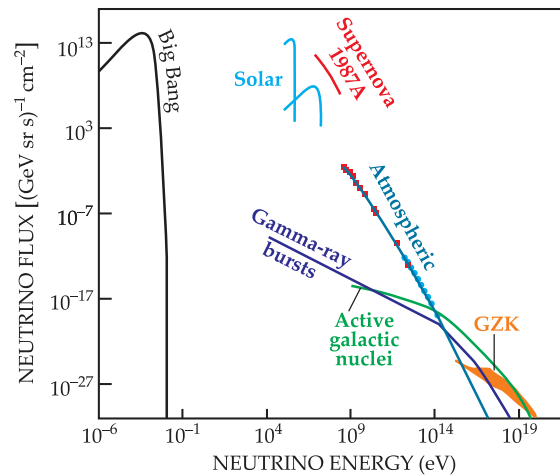


Figure 1.1: Neutrino energy spectrum taken from [HK08]. Cosmogenic neutrinos from the Big Bang can not be detected directly due to their low energies. Solar neutrinos are created in the proton fusion in the core of the sun. Neutrinos from the nearby supernova 1987A are comparable in flux and energy to solar neutrinos. Atmospheric neutrinos are created when cosmic rays hit the atmosphere and follow the energy spectrum of the cosmic rays. Potential sources of high-energy particles, such as gamma-ray bursts and active galactic nuclei, create neutrinos when the particles scatter on other particles or photons. At very high energies particles scatter at the cosmic microwave background, known as Greisen-Sazepin-Kusmin-effect (GZK).

longer than one kilometer [Aar+16]. A tauon can create two showers, one on its creation, and a second one on its decay, as the tauon has a half live of only  $3 \cdot 10^{-13}$  s [PDG18]. In IceCube, electron neutrino showers and muon neutrino tracks have been observed. The search for the tau double-bang is still ongoing [Wil14].

Detectors such as Kamiokande and its successors as well as the Sudbury Neutrino Observatory rely on large tanks placed in mines deep below the surface. While this allows to specifically tailor the Cherenkov medium to the needs of the experiment, such as using highly purified water, it limits the size of the detector.

The earliest approach to use a large natural water volume was done by the DUMAND project, when several strings were deployed near Hawaii in the 1980s. The project was later cancelled due to massive challenges in underwater operation, but provided invaluable insight into the design of later detectors [HK08].

In 1993, a detector consisting of eight strings in Lake Baikal was able to measure the atmospheric neutrino flux. The current generation of this detector is the Gigaton Volume Detector, which is currently under construction. Lake Baikal provides a unique location for a large volume detector, as its water is among the clearest sweet waters of the Earth, corrosion is due to the limited salt content only a minor problem, and deployments of

[Aar+16] M. G. Aartsen et al. "Observation and Characterization of a Cosmic Muon Neutrino Flux from the Northern Hemisphere using six years of IceCube data". In: *Astrophys. J.* 833.1 (2016), p. 3. doi: 10.3847/0004-637X/833/1/3. arXiv: 1607.08006 [astro-ph.HE]

[Wil14] Dawn Williams. "Search for Ultra-High Energy Tau Neutrinos in IceCube". In: *Nucl. Phys. Proc. Suppl.* 253-255 (2014), pp. 155-158. doi: 10.1016/j.nuclphysbps.2014.09.038



Figure 1.2: Left: An IceCube Digital Optical Module is deployed into a hole molten into the Antarctic glacier. Image courtesy of Mark Krasberg, IceCube/NSF. Right: Deployment of a module for the Gigaton Volume Detector at Lake Baikal. Only the surface of the lake is frozen. Image by [Hen] .

strings can be done in late winter, when the lake freezes. Complicated operations like the assembly of the strings can therefore be done on firm ground [HK08].

The AMANDA detector at the Geographic South Pole started operation in 1996. Operation in ice had the advantage of no bioluminescence or K-40 decays as one would expect in a natural liquid water reservoir. Furthermore, corrosion is not a big problem for the equipment. Holes were drilled with hot water into the Antarctic glacier and 19 strings were deployed. It turned out that in the deep ice absorption lengths of up to 200m are possible, making it much clearer than any liquid water source [HK08]. On the basis of AMANDA the IceCube detector was built. A detection volume of one cubic kilometer of ice is instrumented with 5160 optical modules on 86 strings.

## 1.4 Relevant environment parameters for neutrino telescopes

The detection capability of a neutrino telescope is given by various parameters, some of which we will shortly list and give a simplified account on their effect on the telescope.

The total volume determines the detection capability for high-energy neutrinos. Events created by ultra-high-energy neutrinos can easily extend over several kilometers. However, their energy can only be measured, if the event is contained within the detector.

The detection of low energy neutrinos is determined by the spacing of the optical modules and the absorption length of the medium. As low energy events create less light, the modules have to be placed in a denser formation if the absorption length of the medium is short. If the absorption length is high, fewer modules per unit volume can still maintain a good low energy resolution.

As neutrino events are always low in statistics, the background from the medium itself should be as low as possible. Natural liquid water reservoirs always have some degree of

bioluminescence, and, in the case of salt water, K-40 decays.

With muons from atmospheric showers being able to penetrate several kilometers, the position of the detector is also of enormous importance. IceCube at the Geographic South Pole has a very clear view of the Northern neutrino sky, using the Earth as shield against muons. A strong argument can therefore be made for new detectors on the northern hemisphere, complementing IceCube and giving us a clear view of the full sky.

## Chapter 2

# Ocean Networks Canada

### 2.1 Overview

Ocean Networks Canada (ONC), an initiative of the University of Victoria provides the infrastructure for various scientific sub-sea experiments, specifically the supply of electrical power and an Ethernet-based data connections at the sea floor; as well as assistance in the development of sub-sea modules, and the deployment of these. Its two main observatories are VENUS at lower depths in the Salish Sea, and NEPTUNE at high depths in the northeast Pacific ocean. Additional smaller observatories are located in the Arctic Sea, Hudson Bay and the Bay of Fundy. An overview of the observatories is given in Fig. 2.1 gives a brief overview of the observatories of ONC. Several hundred gigabytes of data taken from thousands of individual instruments are accessibly to scientists and the public over Oceans 2.0, an extensive web infrastructure provided by ONC. Apart from supporting physical, chemical, biological and geological experiments, ONC also provides hazard warnings and data relevant for environmental protection [ONC1; ONC2].

The NEPTUNE observatory consists of a 800 km fiber optical cable loop with several nodes. Instrument platforms with junction boxes connect to these nodes, individual instruments connect to the junction boxes. The node at Cascadia Basin is located at 2600 m depth on an abyssal plain, a very flat deep oceanic floor where large amounts of sediment have completely leveled out any geological profile [WT87]. The temperature at Cascadia Basin is at about 2° over the entire year. The currents are very low at 0.1 ms<sup>-1</sup>.

### 2.2 Infrastructure and instrument platforms

Whereas the node at Cascadia Basin is a fixed installation, the instrument platforms are regularly recovered and reequipped. Thus, the deployment of STRAW consisted not only of the deployment of the two strings, but also of the respective instrument platform and other instruments belonging to that platform.

The instrument platform consists of a steel frame with plastic grid walls to which various objects can be fastened. In the middle of the instrument platform a titanium junction box is fastened, which acts as a distributor between node and instruments (Fig. 2.2). Smaller

---

[ONC1] *Ocean Networks Canada Homepage*. <http://www.oceannetworks.ca/>. accessed: 28.10.2018

[ONC2] *Ocean Networks Canada Strategic Plan 2016-2021*. <http://www.oceannetworks.ca/sites/default/files/pdf/ONCStrategicPlan2016-2021.pdf>. accessed: 28.10.2018

[WT87] P. P. E. Weaver and J. Thomson. *Geology and Geochemistry of Abyssal Plains*. London: Geological Society, 1987. ISBN: 978-0-632-01744-7



Figure 2.1: Map of the observatories and stations of Ocean Networks Canada. The STRAW strings are located in the Pacific Ocean, at the location marked for a future neutrino observatory. Image courtesy of Ocean Networks Canada.

instruments can be fastened to the platform and are positioned after deployment by a remotely controlled underwater vehicle (ROV). On two sides of the instrument platform the Teledyne ODI plugs are located. Cables with the corresponding counterpart can be connected to these underwater, as the plug releases a small amount of oil during plugging, thus isolating the connection. The long cables connecting the instruments to the platform, either Kevlar-enforced cables or cables in oil-filled hoses, hang in figure-eight loops on horns at the sides of the platform. This allows the ROV to grab a cable end and fly into position, the cable will unwind from the horns without contortion. The maximum cable length is 70m after which the transmission quality drops significantly.

In some cases instruments do not connect directly to the junction box. In this case an additional intermediary, the mini junction box, is used. The mini junction box is a development by ONC, hosting power converters, Ethernet switches, and microcontrollers for monitoring and controlling the power supply to the instruments. Additionally, the mini junction box contains a fault protection by checking all power lines against a seawater reference. For STRAW, two mini junction boxes were used, one for each string, each equipped with an additional circuit board developed at TUM for timing synchronisation between the instruments.

ONC tests all instruments extensively before deployment. Apart from ensuring that the instruments integrate into the network, several long term underwater tests are done with the main focus on possible leakage and electric faults.

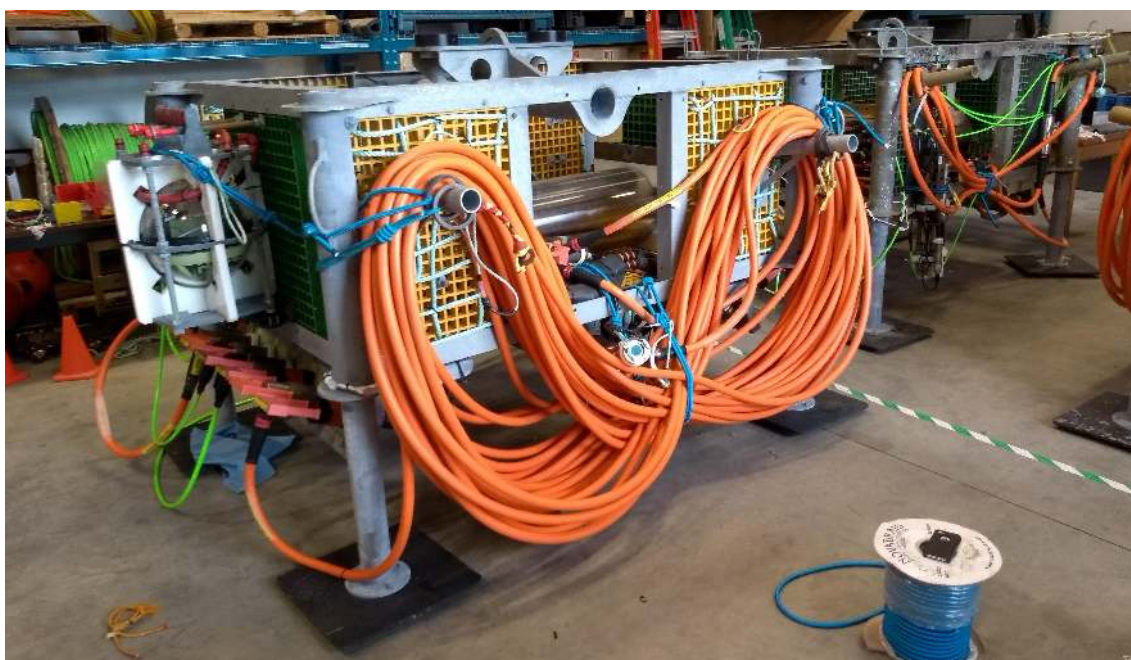


Figure 2.2: Instrument platforms at ONC. In the middle of the steel frame the titanium junction box contains the electronics. On horns on the side an oil-filled hose with data and power cables inside is laid in figure-eight loops. The ODI connectors for the cables (bottom left) are equipped with large handles for ROV interaction. Lighter instruments can be directly attached to the junction box (left: Titan accelerometer). When connecting an instrument the ROV first removes the blue elastic straps holding the orange hose by pulling out the securing pins. It then grabs the free end of the hose and flies to the target instrument. Due to the figure-eight loops the hose unwinds from the junction box without contortion.

### 2.3 Deployment method

For the deployment of instruments, ONC is supported by the Canadian Coast Guard. Using a Coast Guard vessel, instruments are transported to the site. After necessary inspections and maintenance of already existing instrumentation, instrument platforms and instruments are deployed using the heavy lift line of the ship. Final steps for the instrument setup are done on the back deck by ONC personnel. After deployment, a ROV is lowered into the water, inspects the instruments, and makes the necessary connections between instruments, junction box, and node. For the deployment of STRAW, the CCGS John P. Tully served as deployment vessel. The deployment was streamed live and a connection was kept to TUM.

### 2.4 Remotely Operated Platform for Ocean Science (ROPOS)

The ROPOS ROV (Fig. 2.4) by the Canadian Scientific Submersible Factory did the underwater operations during the Tully cruise. Controlled by its own team of operators it is lowered into the water on an umbilical and then navigated using its thrusters. Equipped



Figure 2.3: One of the arms of the ROV. With trained operators the ROV is capable of using these arms almost like human arms, holding tools for performing tasks such as cutting rope or collecting samples.

---

with two mechanical arms and various cameras, it can perform various tasks including collecting samples, using tools like cutters and position instruments. Via the umbilical of the ship it has a thru-frame lift capacity of almost two tons; the arms themselves however can not lift weights over 100kg (Fig. 2.3).



Figure 2.4: ROPOS from the back and the front while in an ONC workshop. On the back side the two main thrusters and part of the buoyancy (yellow) are visible. From the front we see the two arms (one covered by the ladder). Between the arms is a tray on which during missions a box for tools and samples is placed. Various cameras and spotlights guarantee good visual overview during mission.

## Chapter 3

# Simulations and expected environment

Before the planning of our strings, it was vital to estimate the environment, namely the scattering and absorption length would influence our detector geometry, and the background rate, as we would have to tailor our readout electronics to it.

### 3.1 Water transmittivity

The intensity  $I(x)$  of a narrow light cone in water can be described by using an exponential absorption law with  $l_{\text{att}}$  the attenuation length,  $l_{\text{abs}}$  the absorption length, and  $l_{\text{scat}}$  the scattering length:

$$I(x) = \frac{I_0}{4\pi x^2} \exp\left(-\frac{x}{l_{\text{att}}}\right) = \frac{I_0}{4\pi x^2} \exp\left(-x \left(\frac{1}{l_{\text{abs}}} + \frac{1}{l_{\text{scat}}}\right)\right) \quad (3.1)$$

We distinguish between the scattering length  $l_{\text{scat}}$  and the effective scattering length  $l_{\text{scat,eff}}$ . The scattering length describes the length after which a photon has been scattered with a probability of  $1 - 1/e$ . The effective scattering length takes into account the average scattering angle. Especially when Mie scattering on large particles is dominant, the angular distribution has a strong forward preference. The scattered photon therefore often has only a minimal direction change [ANT05]. The effective scattering length corrects for this with the average cosine of the scattering angle  $\theta$ :

$$l_{\text{scat,eff}} = -\frac{l_{\text{scat}}}{\ln \langle \cos \theta \rangle} \quad (3.2)$$

Whereas the scattering length is used for measurements with a narrow beam, as everything scattered by only a few degrees is lost to the beam, the effective scattering length is the relevant parameter when measurements with an isotropic light source are made.

In general, all of these lengths depend on the wavelength. Water, regardless of the site, has a clear transmission window in the visible spectrum with its peak in the blue-green. The relative transmission of wavelengths to each other is mostly constant, however, the absolute values change heavily. This observation by Bradner [DUM] and Jerlov [Jer76] is

---

[ANT05] ANTARES Collaboration. “Transmission of light in deep sea water at the site of the Antares neutrino telescope”. In: *Astropart.Phys* 23 (2005), pp. 131–155. doi: 10.1016/j.astropartphys.2004.11.006

[DUM] H. Bradner for the DUMAND Collaboration. *Attenuation of light in clear deep ocean water*. [http://www.inp.demokritos.gr/web2/nestor/www/2nd/files/247\\_252\\_bradner.pdf](http://www.inp.demokritos.gr/web2/nestor/www/2nd/files/247_252_bradner.pdf)

[Jer76] N.G. Jerlov. *Marine Optics*. Amsterdam: Elsevier, 1976. ISBN: 978-0-080-87050-2

only true for deep sea waters, in coastal waters the relative transmissions can vary.

[Cap+02] have measured the transmission of several sites off the Italian coast in the Mediterranean using an WetLabs AC9 transmissometer and have found attenuation lengths of 50m for blue light (412nm) with a strong tendency for clearer water with greater depth.

Measurements done by the ANTARES collaboration [ANT05] show comparable values. Smith and Baker [SB81] have done measurements of pure sea water, cleaned from dust particles, and made an extensive comparison of the measured values of other experiments. They also agree on a maximum attenuation length of 50m in the best case.

To the knowledge of the author, measurements of the deep Pacific water close to Cascadia Basin have not been conducted so far, extensive measurements of surface water have been done by Jerlov [Jer76]. Jerlov has characterized water into five coastal types and five ocean types. His characterization of the Mediterranean surface water (Type IA) is in good agreement with the previously mentioned measurements; the Canadian pacific coast (Type III) has a four times shorter attenuation length, but this result must not necessarily extend to the water at 2.5km depth.

Based on these results, we assume an attenuation length between 15m and 50m. The modules on our strings are therefore spaced at about 20m with a string distance of 40m and an effective string length of 110m. With this setup the distances between the modules extend over few attenuation lengths in any expectable case.

In Fig. 3.1 we plotted the number of photons we expect to see in an SDOM for a POCAM flash with  $10^9$  emitted photons. The data is based on an absorption spectrum taken from [SB81]. While the absolute values may change depending on the absorption length at the site, the overall picture gives us a good estimate of the dominant wavelengths.

### 3.2 The string in the current

A simulation was written in which the string with a buoyancy at the top is subjected to the expected current of  $0.1 \text{ ms}^{-1}$ . At the time of the simulation, the final setup of the string was not yet fixed, but adequate estimates of the relevant parameters, weight and effective area, could already be made. Fig. 3.2 shows the results of the simulation. For a buoyancy of 300kg the string is displaced at the top by 4m, whereas for 600kg this drops to 1.2m. A large displacement would alter the distances between the modules significantly, thus distorting the absorption length measurement. Allowing a small buffer in case parts of the string should become heavier than expected, a buoyancy of 500kg was deemed to be a good value for an acceptable string tilt.

### 3.3 Preliminary light simulation

In order to obtain information about feasible detector geometries, the light propagation in water was simulated. This simulation allowed us to estimate the effect of shadows, caused e.g. by module mountings, the absolute intensity, and the ratio between scattered and direct POCAM light received by a SDOM detector.

---

[Cap+02] A. Capone et al. "Measurements of light transmission in deep Sea with the AC9 transmissometer". In: *Nucl.Instrum.Meth.* A487 (2002), pp. 423–434. doi: 10.1016/S0168-9002(01)02194-5

[SB81] R. C. Smith and K. S. Baker. "Optical properties of the clearest natural waters". In: *Applied Optics* 20 (2 1981), pp. 177–184

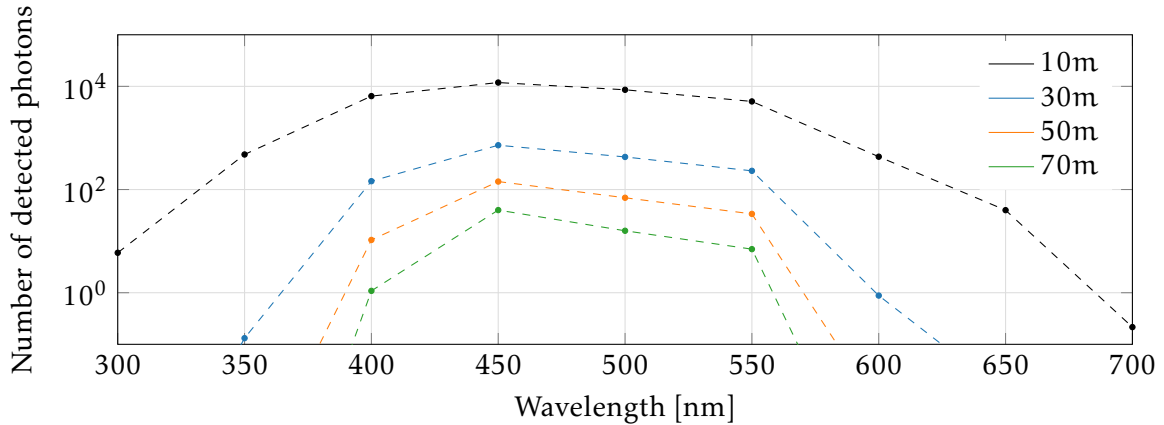


Figure 3.1: By using data from [SB81] we can estimate the light measured by a SDOM when a POCAM pulse creates  $10^9$  photons. The efficiency of the photomultiplier of the SDOM is already factored in. We see that for long ranges significant amounts of light can only be detected in a small window from 450 – 550 nm.

The code written for this simulation uses Mie scattering. Rayleigh scattering, being only a special case of Mie scattering with very small particles (molecules) is not treated separately. Mie scattering describes the scattering of light in a medium, in which many small spherical particles of a different refraction index are suspended [Mie08].

Because it is highly difficult to write numerically stable code describing Mie-scattering, the BHMIE code by Bohren and Huffman [BH98] was used. The Fortran code by Bohren and Huffman providing the scattering profile was compiled and linked to a propagation simulation written in C++.

In general, the scattering of light in water is not the scattering on one type of particle, but the scattering on many particles of different sizes, such as the water molecules themselves (Rayleigh scattering) and various dust particles. For later data analysis the simulation can easily be extended to this functionality; for the preliminary simulation, we only simulated one type of particle at a time.

An early simulation simulated one POCAM and one SDOM at a set distance and orientation to each other. Due to the many possible orientations and distances this approach has turned out to have little explanatory power and high computing power consumption.

To get a better overview over the parameter space the simulation was therefore changed as follows: We no longer simulated two modules, instead only one POCAM is simulated. The SDOM response could then be calculated looking at the angular distribution of the POCAM light at a given distance and factoring in the effective area of the SDOM at a given orientation. The disadvantage of this method is the neglect of the angular dependence of the SDOM photomultipliers. For later data analysis this has to be factored in again, for the preliminary simulation the results are nonetheless sufficient to rule out or favor

[Mie08] Gustav Mie. “Beiträge zur Optik trüber Medien, speziell kolloidaler Metallösungen”. In: *Annalen der Physik* 330.3 (1908), pp. 377–445. doi: 10.1002/andp.19083300302

[BH98] Craig F. Bohren and Donald R. Huffman. *Absorption and scattering of light by small particles*. 2nd ed. Wiley, 1998. ISBN: 978-0-471-29340-8

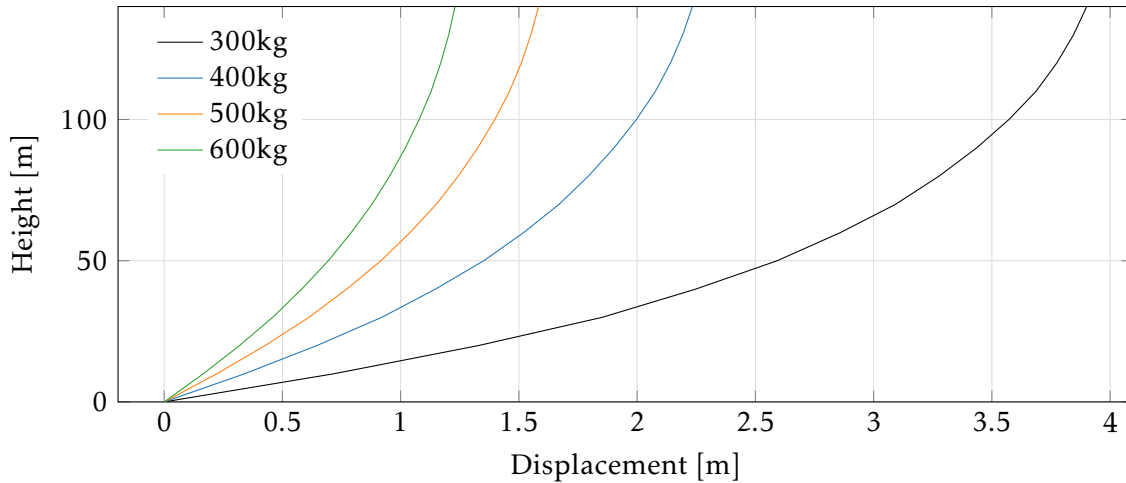


Figure 3.2: Horizontal displacement of the string depending on the buoyancy. At the time of the simulation the final setup of the string was not yet fixed, but adequate estimates for weight and effective area were already available. The simulation assumes a current of  $0.1 \text{ ms}^{-1}$ .

certain detector geometries.

Fig. 3.3 and Fig. 3.4 show exemplary simulations for  $\lambda_{\text{abs}} = 50 \text{ m}$ ,  $\lambda_{\text{scat}} = 100 \text{ m}$  and very small particles (Rayleigh scattering). Many simulations have been done, varying the parameters within the values that could be expected at Cascadia Basin. We do not show the individual results here, as they all more or less match the results shown in Fig. 3.3 and Fig. 3.4. The following conclusions can be drawn for all reasonable parameter sets.

First, the separation between scattered and unscattered light, and thus the calculation of the scattering length, can be extremely difficult. Using a detector placed below a POCAM flashing only its upper hemisphere could be helpful, as all light detected here is scattered. We can compare this intensity to the measured intensity of a detector placed at the same distance above the POCAM, directly looking at the flashing hemisphere, and thus separate absorption and scattering. For the detector this can be realised either by two SDOMs at the same distance, but above and below a POCAM, or by one POCAM and one SDOM, when the POCAM flashes its hemispheres separately.

The second conclusion from the plots is that shadows cast by parts of the module mounting or the strings themselves pose a big problem, as they are neither smeared out to negligibility by scattering, nor sharp enough, so that they could be easily factored out of the measured data by analytical means. This poses large restrictions on the mechanical design of our string. Obviously the module mounting should cast as small a shadow as possible. Additionally, the strings can not be allowed to twist, as this would mean that steel rope and data cables would cast shadows between the modules. As a simple example modules mounted to the side of two single steel wires strings can be considered. With the water current all modules would rotate to the same side, as for example wind vanes do. If the current were constant, we could place both strings perpendicular to the current direction and the modules would have a clear line of sight to each other. However, when the current direction is parallel to the line connecting the strings, meaning that one

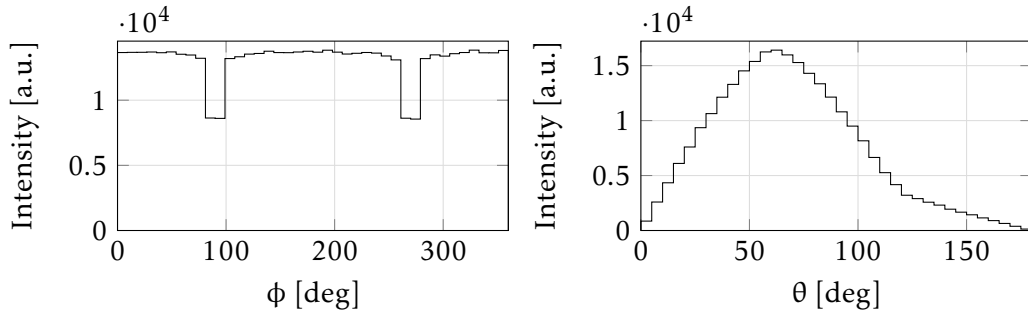


Figure 3.3: A simulation of the POCAM in water with Rayleigh scattering,  $\lambda_{\text{abs}} = 50\text{m}$ ,  $\lambda_{\text{scat}} = 100\text{m}$ . The light output was observed at 50m distance. Left: both hemispheres are flashing, the light distribution in  $\phi$  was plotted. The POCAM was held between two steel wires casting shadows. We see that the shadows are blurred and the blur extends over about  $60^\circ$ . Right: light distribution in  $\theta$  for a POCAM flashing only one hemisphere.

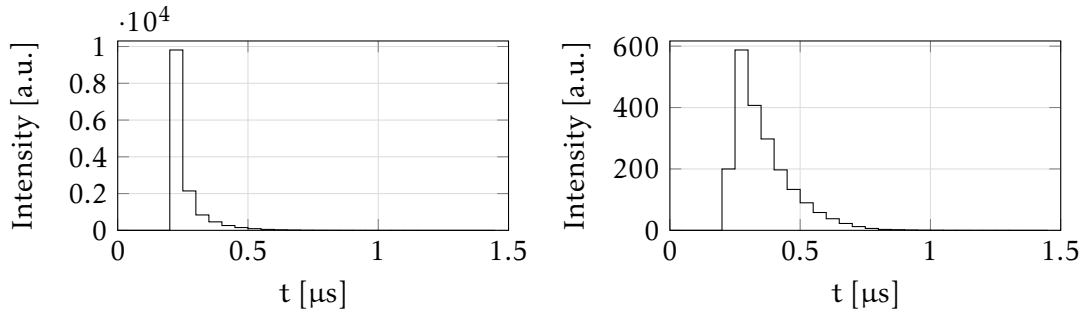


Figure 3.4: Simulation with the same parameters as in Fig. 3.3. Only the upper hemisphere is flashing. Left: time distribution of the light at 50m distance for  $\theta < 20^\circ$ . We see a sharp peak of direct light with a comparatively small tail of scattered light. Right: time distribution for  $\theta > 160^\circ$ . Below the POCAM we see only scattered light. Both histograms use the same scale on the y-axis.

string is behind the other, with all modules flowing behind their strings, the line of sight is clearly blocked by one of the strings. Data provided by ONC shows that the current at Cascadia Basin changes over the year and has no preferred direction. Thus, strings resistant to rotation had to be developed.

## Chapter 4

# The double string

As the previous chapter about preliminary light simulations showed, the strings need some stability against twisting. It was unfeasible to make the strings out of a single steel line that would by itself be stiff enough to resist twisting caused by the water current. This single line would be extremely heavy and too stiff to be handled conveniently on the ship. Instead many steel lines can be used to build a string. In the easiest configuration two steel lines run parallel and are connected by spacers, which are stiff steel bars keeping the lines apart at a fixed distance. The STRAW strings follow this design, two steel lines run at 0.4m distance. Every 5m a steel spacer clamps to both lines and keeps them at 0.4m distance. This concept can be compared to a rope ladder.

With such a design the resistance against twisting is provided by the fact that twisting will shorten the double line, thus a strong buoyancy at the top, pulling on the string, results in a certain string stiffness. It could be argued that the stiffness of steel ropes themselves adds additional stiffness to the double line. However, it is very difficult to lay out a long steel rope without any twists. Thus it becomes equally impossible to assemble a string that has not a predisposition to twist in some direction, especially as one has to consider that a twist-free steel rope might want to twist once tension is applied. Thus the approach is to use steel ropes that have as little as possible stiffness themselves and provide all of the string stiffness by a large buoy at the top. The stiffness of a double string can be adjusted by the distance between the parallel wire ropes and the distance between the spacers. Precise calculations are presented in Chapter 7.

Of course the stiffness could be improved by adding more lines to a string. A triple string was considered, based on three steel ropes kept apart by triangular spacers. The idea was discarded, as, unlike a single string or a double string, a triple string could not be rolled up. Thus, storage, transportation, and deployment would have been significantly more complicated.

On a double string the modules can either be positioned between the two steel ropes or outside the steel ropes (Fig. 4.1). Positioning them in-between allows for a lighter mounting. Positioning them outside requires a heavy mounting, adds the problem of tilt, as the center of mass is no longer between the steel ropes, and provides bigger leverage for the water current to twist the string, as the modules are the parts with the largest drag. However, the big advantage of placing the modules outside is that the steel ropes and data cables, whose shadows could disturb the measurements, are now on only one side of the module. Thus the string could theoretically twist up to a value slightly below  $180^\circ$  before the shadows would pose a problem. With the module between the steel ropes shadows become a problem if the twist reaches a value close to  $90^\circ$ .

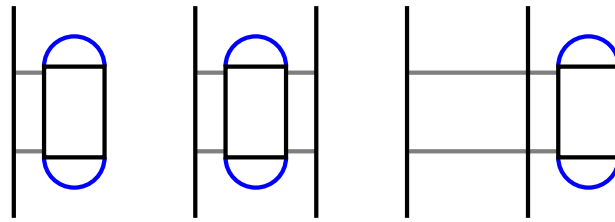


Figure 4.1: Possible string configurations. Left: a single wire rope, allowing the module to rotate freely in the current. The stiffness of the wire rope can be neglected on a length of up to 110m. Middle: a module mounted between two wire ropes. Rotation is no longer possible. Right: a module mounted to the side of two wire ropes. Rotation is not possible and only one shadow is cast, as wire ropes lie in the same line of sight.

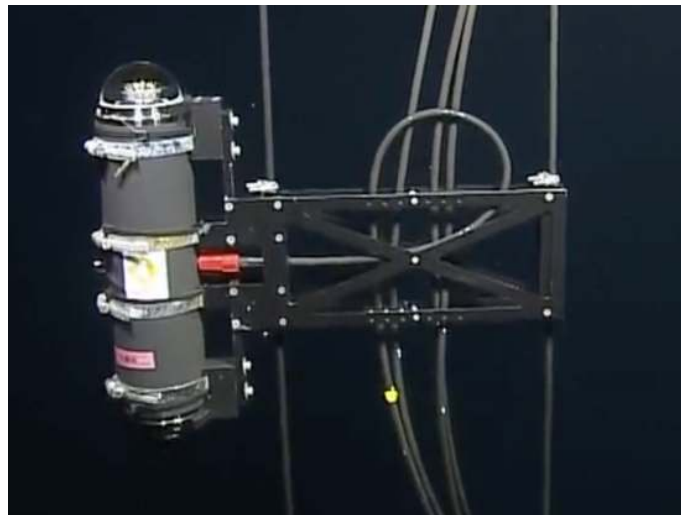


Figure 4.2: Double string and module mounting of STRAW at Cascadia Basin. Image taken by the ROV after deployment.

At the same time as the string structure was developed we also considered the deployment mechanism. The concept of the winch, which is extensively described in Chapter 9, was developed. On a winch having the modules between the steel ropes means that successive layer spooled onto the winch cover the modules, thus accessing them after the string has been spooled becomes extremely difficult. If the modules are placed outside of the steel ropes they would still be accessible on the winch.

Considering the last two arguments it was decided that the modules would be best placed outside of the steel ropes (Fig. 4.2).

## Chapter 5

# Modules

### 5.1 POCAM

The Precision Optical Calibration Module (POCAM) is an isotropic light source developed as a calibration device for IceCube Gen2 [Jur+16]. A previous version has already been successfully tested in the Gigaton Volume Detector in Lake Baikal [Spa17]. At its center are two semi-transparent PTFE (teflon) integrating spheres, which diffuse the light of fast pulsed LEDs.

#### 5.1.1 Housing

Designed to withstand the freezing pressure at the South Pole, the housing consists of a titanium cylinder with two BK-7 glass hemispheres at a total length of 40 cm and a rating of 1500 bar. In each hemisphere one integrating sphere illuminates  $2\pi$ . At large distances the light output of both hemispheres merges to an almost isotropic  $4\pi$  illumination. The glass hemispheres are glued to titanium flanges which are bolted to the main cylinder. A vacuum plug for evacuation and an electrical plug penetrate the cylinder at opposite sites (Fig. 5.3).

#### 5.1.2 Integrating sphere

The integrating sphere was manufactured at TUM based on Geant4 simulations [Gär16] and measurements [Hen18]. Using the special property of teflon to have a diffuse cosine reflection (Lambertian reflection) as well as a diffuse cosine transmission at low thicknesses, a teflon sphere can completely diffuse the light of a light source with an arbitrary emission profile (Fig. 5.4). The teflon sphere in the POCAM has a diameter of 50 mm and a thickness of 1 mm and is placed above an array of six LEDs. Directly above the LEDs the

---

[Jur+16] M. Jurkovič et al. “A Precision Optical Calibration Module (POCAM) for IceCube-Gen2”. In: *EPJ Web Conf.* 116 (2016), p. 06001. DOI: 10.1051/epjconf/201611606001

[Spa17] Christian Spannfellner. *Realisierung des ersten Precision Optical Calibration Modules für das Gigaton Volume Detector Neutrino Teleskop in Baikal*. BA thesis, [https://www.cosmic-particles.ph.tum.de/fileadmin/w00bk1/www/Thesis/BA\\_Christian\\_Spannfellner.pdf](https://www.cosmic-particles.ph.tum.de/fileadmin/w00bk1/www/Thesis/BA_Christian_Spannfellner.pdf). July 2017

[Gär16] Andreas Gärtner. *Realization of the “Precision Optical Calibration Module” prototype for calibration of IceCube-Gen2*. BA thesis, [https://www.cosmic-particles.ph.tum.de/fileadmin/w00bk1/www/Thesis/gaertner\\_BA.pdf](https://www.cosmic-particles.ph.tum.de/fileadmin/w00bk1/www/Thesis/gaertner_BA.pdf). July 2016

[Hen18] Felix Henningsen. “Optical Characterization of the Deep Pacific Ocean: Development of an Optical Sensor Array for a Future Neutrino Telescope”. MA thesis. Technical University of Munich, July 2018

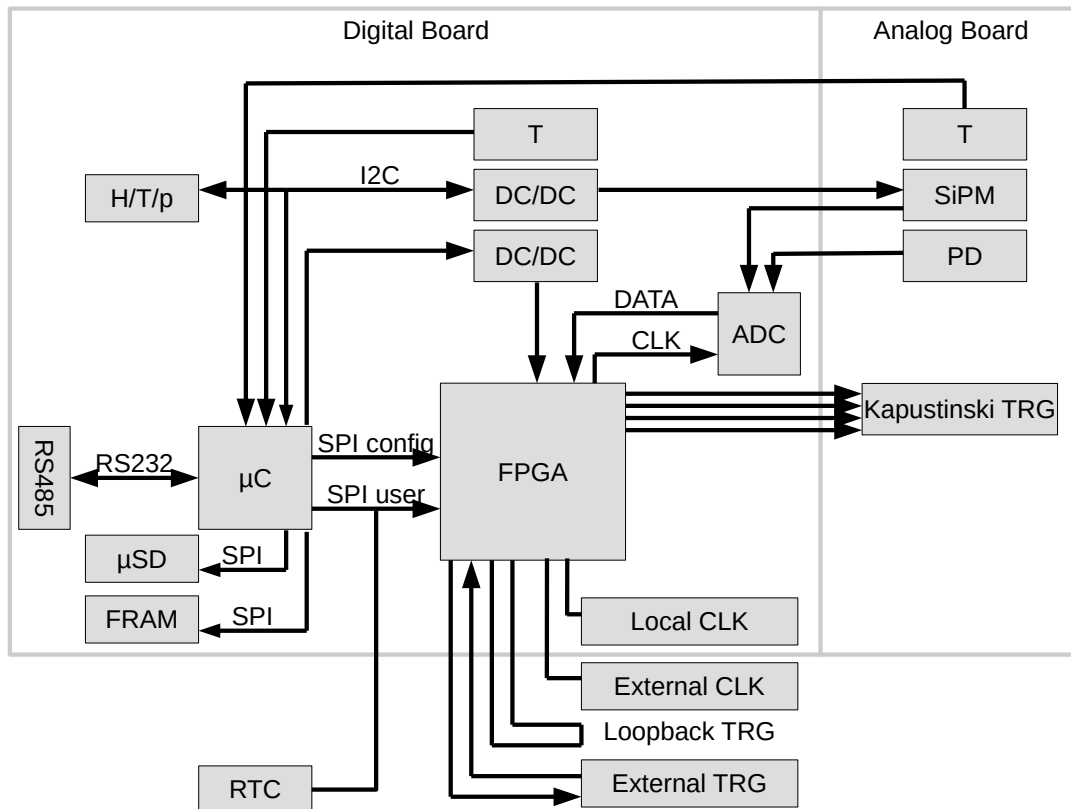


Figure 5.1: Scheme of the electronics of one POCAM hemisphere developed by M. Böhmer of ZTL. A microcontroller handles communication and data storage, a FPGA deals with sensor readout and LED triggering. Apart from the silicon photomultiplier (SiPM) and the photo diode (PD) several environment sensors were used for temperature (T), pressure (p), and humidity (H). A trigger signal from one FPGA travels to the other FPGA (External TRG) and through a cable of the same length back to the original FPGA (Loopback TRG), thus allowing synchronized triggering.

thickness of the sphere is only 0.5 mm in order to increase light yield. A detailed study on the emission profile has been done in [Hen18].

### 5.1.3 In-situ calibration

Per hemisphere the POCAM has two sensors, a photo diode and a silicon photomultiplier, monitoring the light output. This allows us to compensate to some extent effects such as temperature changes and aging of components. Before readout, the signals are amplified using a Cremat charge amplifier.

### 5.1.4 Electronics

The electronics of the POCAM were developed by Michael Böhmer of ZTL. Inside the POCAM circuit boards are stacked on each flange (Fig. 5.2). The two hemispheres of the

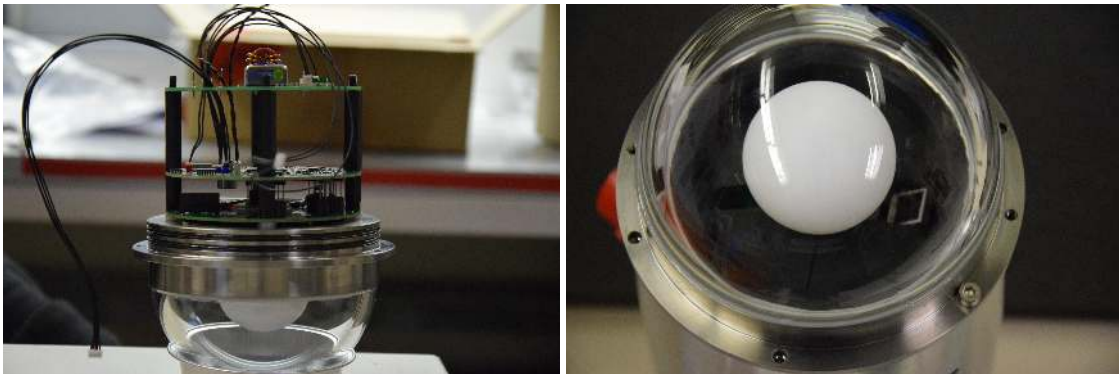


Figure 5.2: Left: stacked circuit boards of a POCAM hemisphere. From top to bottom: power board, digital board, analog board. Right: closeup view of one hemisphere on a closed POCAM. Below the integrating sphere a piece of aluminium coated in a black low gloss color with openings for the sensors. [Hen]

POCAM can operate independent of each other ensuring maximum redundancy. The data connection to the outside is RS-485, the same protocol that was used for the Gigaton Volume Detector. It is therefore the only module that can be more than 70m away from a mini junction box, which is the limiting distance for Ethernet communication through the sub-sea cables. The RS-485 signal goes to each of the digital boards, one per flange, holding a microcontroller for communication, data storage and slow control, as well as a FPGA for sensor readout and LED triggering. The LEDs are driven by a Kapustinsky circuit. Both microcontroller and FPGA can be updated remotely if necessary. The digital board is stacked onto the analog board holding LEDs, Kapustinsky circuits, sensors, and amplifiers. One central power board creates the necessary voltage for the microcontrollers and houses the central clock. The FPGAs of both hemispheres have a direct connection, allowing, after one has been set up as master and one as slave, a synchronized light pulse from both hemispheres (Fig. 5.1).

### 5.1.5 Kapustinsky circuit

The LED driver, providing pulses of  $10^9$  photons at pulse lengths of below 10 ns, is based on the design of Kapustinsky [Kap+85] with the modification proposed by [LV06]. The Kapustinsky flasher is based on a quick discharge of a capacitor through a LED, with an inductance parallel to the LED shortening the pulse.

F. Henningsen of the STRAW team has done an extensive experimental characterization of the impact of the inductance, the capacity and the voltage on the circuit as well as a test of various LEDs, which have a significant impact on the pulse length. [Hen18]

[Kap+85] J.S. Kapustinsky et al. "A fast timing light pulser for scintillation detectors". In: *Nuclear Instruments and Methods in Physics Research Section A: Accelerators, Spectrometers, Detectors and Associated Equipment* 241.2 (1985), pp. 612–613. ISSN: 0168-9002. DOI: 10.1016/0168-9002(85)90622-9. URL: <http://www.sciencedirect.com/science/article/pii/0168900285906229>

[LV06] B. K. Lubsandorzhev and Y. E. Vyatchin. "Studies of 'Kapustinsky's' light pulser timing characteristics". In: *JINST 1,T06001* (2006)

[Hen18] Felix Henningsen. "Optical Characterization of the Deep Pacific Ocean: Development of an Optical Sensor Array for a Future Neutrino Telescope". MA thesis. Technical University of Munich, July 2018

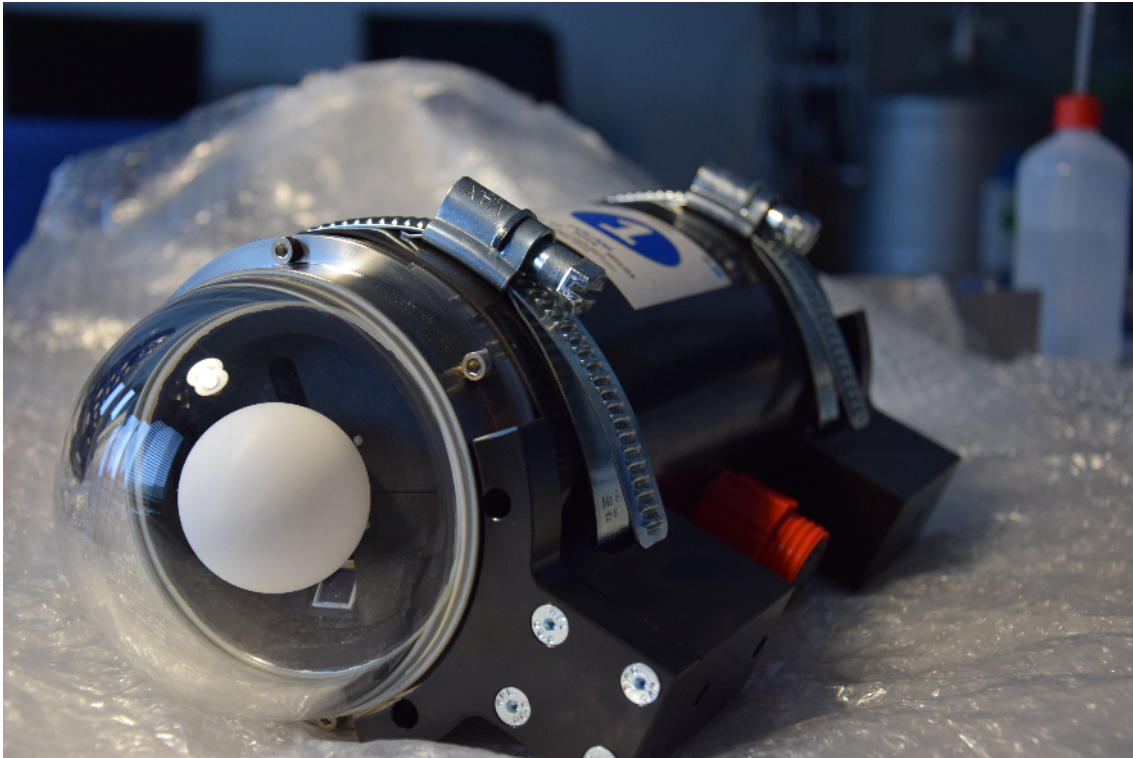


Figure 5.3: An assembled POCAM already wrapped in Viton and clamped to the POM parts which will later hold it to the string. The red plastic jacket of the electrical connector is clearly visible. [Hen]

## 5.2 SDOM

The SDOM is a newly developed instrument for STRAW. It uses two photomultiplier tubes to detect photons; measurements from different SDOMs are synchronized with 10 ns precision. Its purpose is the measurement of background radiation caused by radioactivity and bioluminescence as well as the detection of POCAM flashes, which can be used to determine absorption and scattering length.

### 5.2.1 Housing

The SDOM uses the same housing as the POCAM with a longer titanium cylinder, thus having an overall length of 60 cm. The usual optical module housing in neutrino detectors is a single large glass sphere. We chose to use the titanium cylinder setup as this allowed for simpler mechanics, the fastening mechanism to the string could be almost the same for the different modules, and provided a more convenient solution for opening and closing the modules with the flanges (Fig. 5.5).

### 5.2.2 Photomultiplier

The SDOM uses two Hamamatsu 3" photomultiplier tubes, one looking up, one looking down, each with a high voltage base. All used PMTs have been characterized by I. C. Rea

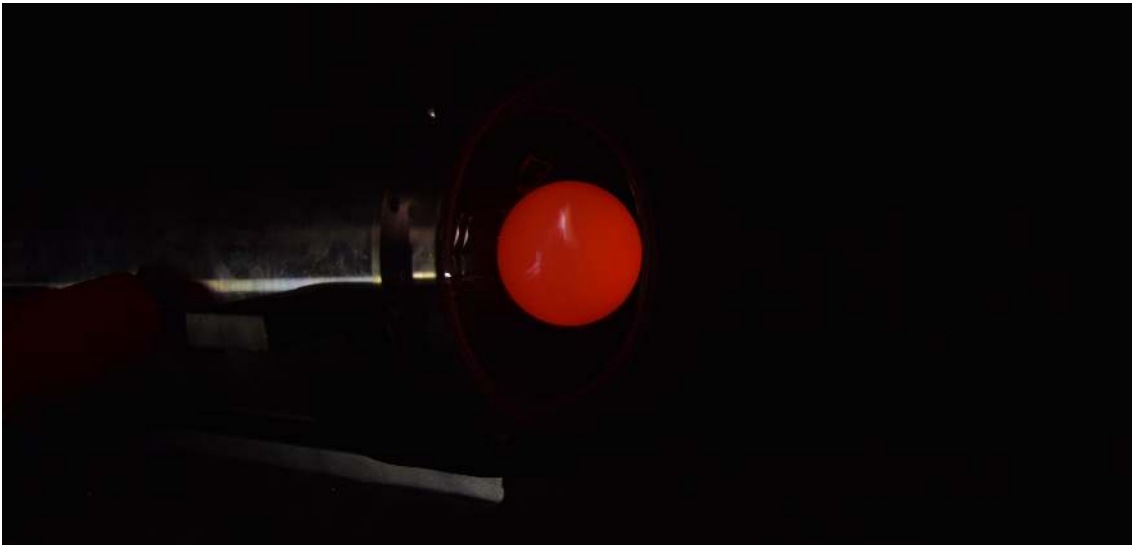


Figure 5.4: The integrating sphere inside the POCAM diffuses light to an almost isotropic emission. For measurements the POCAM was placed in a dark box. [Hen]

of ECP for relevant parameters, such as dark count, gain and transit time spread.

### 5.2.3 Electronics

For data readout a TRB3sc and a Padiwa3 board developed at GSI were used. The TRB3sc is a front-end for various extensions, giving picosecond precision timing, triggered data readout, and slow control. The Padiwa3 is connected to the TRB3sc and provides a multi-level time-over-threshold measurement. By using voltage and current dividers the signal of each PMT was split to four levels, each of which was measured by the Padiwa. With this setup we can make time-over-threshold measurements for four thresholds per PMT.

Multiple TRB3sc can be connected (TrbNet) to provide synchronized time measurements. However, for synchronization a 2Gbit fibre connection is needed, which is not available in STRAW. M. Böhmer of ZTL developed an alternative method for synchronisation by copper wire. A central device, located inside both mini junction boxes, sends differential pulses with varying length to all TRB3sc in all sDOMs, where the pulses are measured by time-to-digital converters (TDC), and recorded by the trigger circuit inside the TRB3sc. This allows event assembly across all sDOMs during the later analysis via software. A small Linux computer in each SDOM reads the TRB data and stores it locally. Timing calibration is therefore provided by checking the SDOM signal against the pulse length of the synchronization signal in the measured data, taking into account the signal run time through the data cable.

## 5.3 The Medusa board

The Medusa board by M. Böhmer of ZTL provides the synchronization signal for the SDOM readout. Each string has one Medusa board in its mini junction box (Fig. 5.6). One

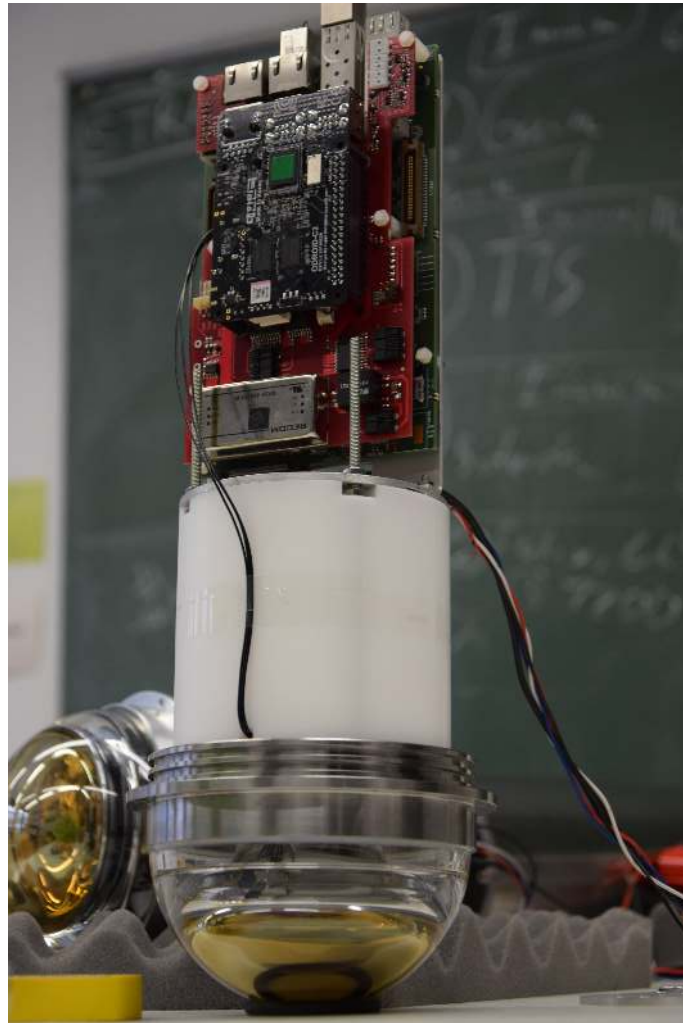


Figure 5.5: Internals of a SDOM. A photomultiplier tube is optically coupled to the glass using optical gel and held in place by a milled POM jacket. An aluminium plate holds TRB3sc, Padiwa, and a computer (Odroid C2). [Hen]

board is set up as master, providing a sync signal to all SDOMs on its string, the other as slave, repeating the signal of the master to the SDOMs on its string. The boards can be configured over a web interface and controlled by sending UDP packets. All signal lines are secured with relays and can be switched off in case of water damage in a module. The synchronization signal uses the LVPECL protocol over a twisted wire pair.

The distribution of a timing signal had a significant impact on the sub-sea wiring of the STRAW setup. As changes to the junction box on the instrument platform could not be made, a direct line between the mini junction boxes was needed. A daisy chain configuration was the preferred way, requiring only two sub-sea connections, one from the instrument platform to the first string and between the strings.

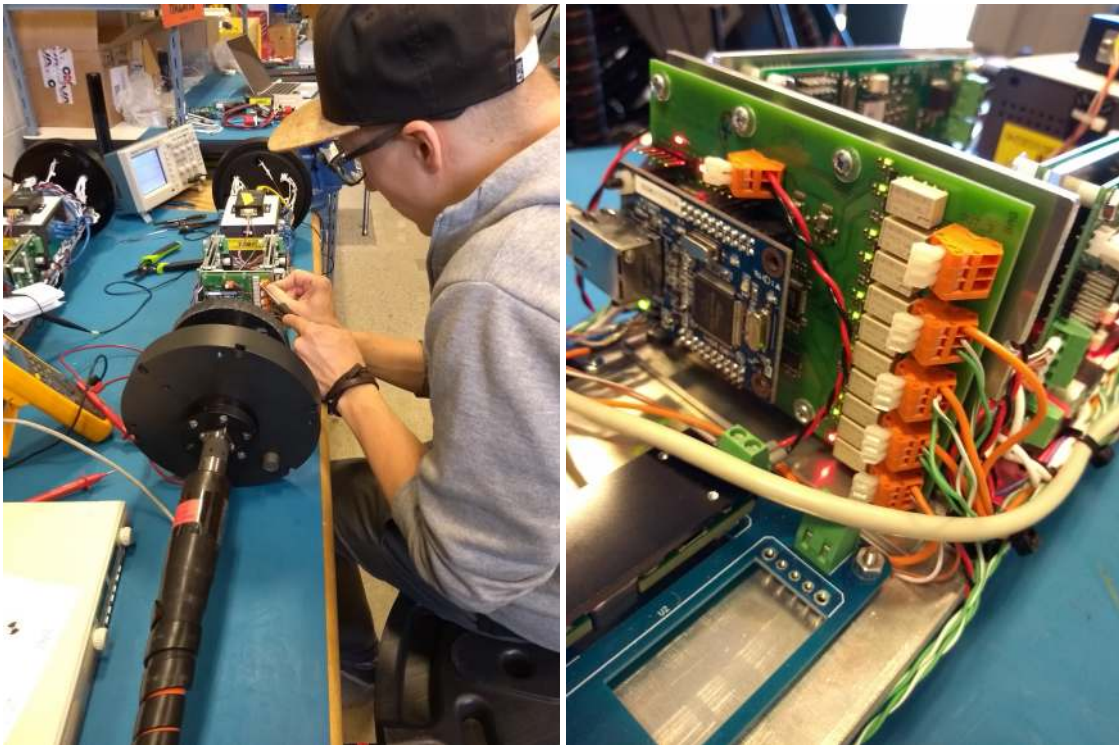


Figure 5.6: Left: C. Spannfellner of ECP mounting a Medusa board in an ONC mini junction box. Right: close-up of the Medusa board. The relays (white boxes) can switch off individual outputs (orange) in case of module failure. The FPGA (black) creates or repeats the sync signal, depending on it being set up as master or slave.

## Chapter 6

# Material choice and corrosion protection

### 6.1 Materials overview

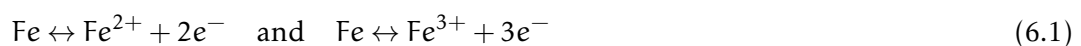
The anchors, provided by Ocean Networks Canada, consist of two massive train wheels each, and a construction steel top, protected by zinc spray paint and sacrificial zinc anodes. The wire ropes of our strings are galvanized steel coated with 1mm polyethylene (Lupolen). The modules (POCAMs and SDOMs) have a titanium housing with BK-7 glass hemispheres. Both of these materials do not corrode in an offshore environment and are not dealt with in this chapter. The module mountings are hot-dip galvanized construction steel coated with a black sub-sea paint coating. The connections to the modules are made from polyoxymethylene (POM) for galvanic isolation. For the same reason the titanium housings were wrapped in large sheets of Viton rubber. All bolts and nuts are electro-galvanized steel.

### 6.2 Steel and steel protection

The standard material for large offshore instructions is steel, due to its mechanical strength and low price. Its main disadvantage is corrosion. The protection of steel parts is therefore paramount for all deep-sea applications. This section will describe the protection mechanisms used during the STRAW installation.

A common method for preventing metal corrosion in sub-sea environments is the use of a second metal, which acts as an anode, where the metal to be protected acts as a cathode in a galvanic cell with the sea water as electrolyte.

The usual corrosion of metal is caused by the reaction of the metal with its non-metallic environment. Chemically speaking this is a redox reaction. The crucial step for cathodic protection is the electron donation; for the specific case of iron:



The balance of these equations can be shifted according to Le Chatelier's principle. Negatively charging the iron will cause the reaction equilibrium to move to the right hand side, positively charging the iron moves the equilibrium to the left hand side. When sufficiently positively charged the corrosion of iron or any metal can therefore be brought to a halt.

The negative charge of the iron is guaranteed by its role as a cathode in a galvanic cell. The same chemical argument shows that the anode is subject to accelerated corrosion and therefore often called the sacrificial anode. Any metal of sufficiently lower electrochemical potential ( $\Delta U = 0.9\text{V}$ ) than iron can act as anode; common choices are zinc, aluminium and magnesium. Extensive information for the design of these anodes can be found in the recommended practice document by Det Norske Veritas [DNV].

The advantages of this form of rust protection are its simplicity, it is enough to bolt a sufficiently large block of zinc to the structure that has to be protected, its mechanical stability and reliability, and the ability to check the rust protection by simple visual inspection of the corrosion progress of the sacrificial anode (Fig. 6.1).

Disadvantages are the creation of aggressive hydroxyl ions  $\text{OH}^-$  at the cathode, which can destroy paint coats. [DNV] states that coats on polyurethane or epoxy basis have shown to be resistant to this effect.

On uncoated parts or parts with damaged coating the cathodic protection leads to  $\text{CaCO}_3$  formation on the bare metal surface, providing effectively a coating.

It must be mentioned that for large structures many distributed sacrificial anodes are needed. A single sacrificial anode at the bottom of the mooring line can not protect it, as the voltage drop along the line can lead to a non sufficient potential at the top.

In our string design Ocean Networks Canada uses zinc anodes to protect the upper parts of the anchors, which provide the connection points to our strings. These parts allow the rotation of the string, which was used for orienting the two strings to face each other with their modules. The massive body of the anchor consist of two train wheels and needs no rust protection due to its sheer size (Fig. 6.2).

Using simple formulae the required amount of zinc has been calculated. According to [DNV] 1 kg of zinc can provide 780 Ah in sea water and 700 Ah in sediment. The top part of the anchor has not sunk into the sediment, we therefore use the first value. The effective mass fraction for cathodic protection is 90% of the original zinc mass. At the depth and temperature of STRAW, the estimated current through the steel surface is  $0.22\text{A/m}^2$  [DNV]. Estimating the surface of the top parts of the anchor to  $1\text{m}^2$  we see that one kilogram of zinc can protect these parts for about four months. ONC used 2.5 kg of zinc per anchor to ensure that rusting would not block the rotating mechanism until the final orientation was done by the ROV.

### 6.3 Different metals in contact

The concept of cathodic protection is to deliberately sacrifice a less noble metal/alloy to protect the nobler metal/alloy. However, the same chemistry often causes failure, when a galvanic cell is created unintentionally. If, for example, two components made from different metals touch, the corrosion of one will be accelerated by orders of magnitude. It was therefore a fundamental design principle of STRAW to never have an electrical connection between different metals/alloys. This principle applies only to parts exposed to sea water, within the modules metal connection is no problem, as in the absence of sea water a galvanic cell can not occur.

Therefore the titanium modules are electrically separated by plastic (POM) parts from their steel mountings.

---

[DNV] *DNV-RP-B401: Cathodic Protection Design*. <https://rules.dnvg1.com/docs/pdf/DNV/codes/docs/2011-04/RP-B401.pdf>, accessed 07.10.18. Det Norske Veritas. Oct. 2010



Figure 6.1: Partially consumed sacrificial anode on recovered ONC equipment. A main advantage of sacrificial anodes is that the rust protection of the steel can be checked by a simple visual inspection of the anode.

## 6.4 Zinc coating

While usually regarded as a separate method for corrosion protection, coating steel parts with zinc provides protection by the principles of cathodic protection. Covering entire steel parts in zinc does not only provide a sacrificial anode but also reduces the steel surface exposed to sea water, ideally reducing it to zero [Leh70].

Zinc based spray paint is the simplest but also the least durable way for coating the surface [Coo70]. It was used by Oceans Networks Canada for parts of the anchor as addition to the zinc anodes.

As a more robust solution the steel parts can be galvanized. Electro-galvanization covers parts in zinc by applying a negative potential and submerging them in a zinc salt solution. Hot-dip galvanization works by submerging the parts in molten zinc. It results in a more abrasion-resistant surface, as the surface is not only covered by a layer of zinc but also by a layer of a hard zinc iron alloy [JOT10]. We chose hot-dip galvanization for the module mountings and spacers for this reason. A disadvantage of this method was that the zinc tended to form drops in the drill holes of our parts and completely closed most holes with a diameter smaller than 10 mm. This effect, while anticipated, was stronger than expected and required a large amount of subsequent re-drilling.

[Leh70] Joseph A. Lehmann. “Cathodic Protection of Offshore Structures”. In: *Jom* 22.3 (1970), pp. 56–63. doi: 10.1007/bf03355632

[Coo70] Albert R. Cook. “The Role of Zinc in the Corrosion Protection of Offshore Structures”. In: *Jom* 22.4 (1970), pp. 40–45. doi: 10.1007/bf03355635

[JOT10] “Was das Feuerverzinken wirklich kann”. In: *JOT Journal für Oberflächentechnik* 50.2 (2010), pp. 34–36. doi: 10.1007/bf03252512



Figure 6.2: Sacrificial anode (flat zinc cylinders) on the left and right of the anchor. The top of the anchor is coated with a zinc spray paint. The train wheel weights are left unprotected.

---

## 6.5 Paint

As an additional layer of rust protection the spacers and mountings were covered in a black polyurethane based color for sub-sea applications. For the winches, the deployment system for the strings, Carboline Carboguard 1209, an epoxy based coating with fiberglass flakes, was applied by hand. The module mountings and the spacers were sprayed with Sika SikaCor EG-5, a coat based on polyurethane and acrylic. SikaCor was chosen as an alternative to CarboGuard, which could not be used in the paint sprayers of the manufacturing workshop. Both paints are two-component paints with high mechanical and chemical resistivity.

## 6.6 Bolts and nuts

Concerning the coating of the nuts and bolts a compromise had to be made between corrosion resistance and practicality. Coating them with paint would have made it difficult to remove them again and this option needed to be kept open, in case problems would arise during the first assembly of the strings. Therefore, off-the-shelf galvanized bolts and nuts were used, even though they were only electro-galvanized, making them the weakest part of our mechanics (Fig. 6.3). Painting them after the string assembly was also not possible due to a lack of a room big enough to let the 130m long strings dry.

To avoid the loosening of the bolts due to vibrations during transport and deployment all screws were secured with Loctite 270, which was chosen after consulting with chemical engineers at Henkel as suitable for subsea applications. Additionally, the small nuts (M4) used for spacers and mountings are all self-locking.



Figure 6.3: Left: Electro-galvanized nuts on the module mountings. The mountings themselves are hot-dip galvanized and painted. Right: Test piece of the polyethylene coated steel wires.

## 6.7 Steel wires

The manufacturer of the two steel wires, which form the backbone of each string, offered to either coat them with paint or with polyethylene (Lupolen). The second option was chosen as it provides a mechanically more resistant cover (Fig. 6.3). Apart from reducing unwanted light reflections and protecting the wire ropes themselves, this coating is also vital for the galvanically protected parts of the string, as an uncoated wire rope would drain their anodes or zinc coatings. The corrosion protection works by covering the surface of the wire ropes and therefore not exposing them to sea water. The terminals at the ends of the wire ropes are galvanized.

## 6.8 Overdesign

A common practise against corrosion is the over-designing of parts. Where weight was of little concern, steel parts were designed to be substantially thicker than needed, thus being able to maintain stability even with large-scale corrosion. Often multiple methods for corrosion protection were used. ECP used hot-dip galvanized parts and additionally coated them with paint, ONC used large sacrificial anodes and zinc spray paint.

## 6.9 Stainless steel corrosion

Stainless steel was not used in the STRAW projects due to its specific corrosion characteristics, namely pitting and crevice corrosion. Whereas construction steel generally corrodes uniformly, which allows for a simple compensation by using thicker parts and/or coating, stainless steel corrosion is, while rare, heavily localized.

The normal insensitivity of stainless steel is caused by a thin passive oxide layer on its surface. In environments with chloride ions  $\text{Cl}^-$ , the chloride can break through this passive layer and start a corrosion nucleus. Due to this reaction the small nucleus becomes the anode of a galvanic cell with the main body of the steel as cathode, which

accelerates its corrosion further. Thus small hemispherical pits are created in the steel. These pits have the size of several micrometers and can passivate again when the surface oxidizes [Fra+87; Kae79]. During this passivation the chloride and iron ions trapped in the pit are set free and increase the probability for nearby pits to form. C. Punckt et al. [Pun04] have found that this process can even under small environment changes reach criticality and a chain reaction of pit creation is started. This chain reaction leads to massive corrosion on a small part of the steel, a process known as pitting. The second form of stainless steel corrosion, the so called crevice corrosion, reflects the fact that narrow crevices, as they occur on pipe joints or bolt connections are specifically prone to corrosion. The model of Stockert and Boehni [SB91] identifies this as the same mechanism as pitting, stabilized by the narrow geometry of the crevice, which as a diffusion barrier keeps the aggressive chemicals released by the pitting inside. Experimental evidence to this model is provided by N. L. Laycock et al. [LSN97].

As these forms of corrosion are hard to predict, occurring only with a very low probability but setting forth a chain reaction of corrosion, thus stainless steel is not the material of choice for offshore applications. Oil and gas industry as well as scientific institutes such as ONC prefer galvanized construction steel. In accordance with their experience we have not used stainless steel for STRAW.

## 6.10 Winch

While the winch was not deployed and therefore did not need heavy rust protection, it was still tested for several days in ONCs salt water test tank, as we tested our strings spooled on the winch. We therefore gave it minimal protection and used it as a test object. Some of its parts are hot-dip galvanized, others paint coated, whereas others were left uncoated. After being recovered from the test tank the winch showed only light rust on some uncovered steel parts. It was rinsed with sweet water before storage.

## 6.11 Choice of colors

Since STRAW is an optical instrument we used black colors to reduce interference with our measurements. The subsea paint used on module mountings and spacers was black as well as the coating of the wire ropes and the POM for the electrical isolators. Where necessary black galvanized nuts and bolts were used.

---

[Fra+87] G. S. Frankel et al. "Metastable Pitting of Stainless Steel". In: *Corrosion* 43.7 (1987), pp. 429–436. doi: 10.5006/1.3583880

[Kae79] Helmut Kaesche. *Die Korrosion der Metalle*. 1979. Chap. Lochfraßkorrosion. doi: 10.1007/978-3-662-11502-2

[Pun04] C. Punckt. "Sudden Onset of Pitting Corrosion on Stainless Steel as a Critical Phenomenon". In: *Science* 305.5687 (2004), pp. 1133–1136. doi: 10.1126/science.1101358

[SB91] L. Stockert and H. Böhni. "Susceptibility to Crevice Corrosion and Metastable Pitting of Stainless Steels". In: *Materials Science Forum* 44-45 (1991), pp. 313–328. doi: 10.4028/www.scientific.net/msf.44-45.313

[LSN97] N.j. Laycock, J. Stewart, and R.c. Newman. "The initiation of crevice corrosion in stainless steels". In: *Corrosion Science* 39.10-11 (1997), pp. 1791–1809. doi: 10.1016/s0010-938x(97)00050-4



Figure 6.4: Polyoxymethylene (POM) isolators on the module mountings

---

## 6.12 Non-metallic components

To avoid metal contact between the steel mountings and the titanium modules electrically isolating parts were needed. While little information was available on plastics for deep-sea application, the Saechtling Kunststoff Taschenbuch [BOR10] lists polyoxymethylene (POM) as a synthetic material of low water absorption and high resistivity against solvents, light acids and lyes and anorganic salts. Due to its machining properties it was chosen as a isolating metal substitute (Fig. 6.4). Additionally, the titanium modules were wrapped with a Viton sheet.

---

[BOR10] E. Baur, T. A. Osswald, and N. Rudolph. *Saechtling Kunststoff Taschenbuch*. Hanser, 2010. ISBN: 978-3-446-43442-4

## Chapter 7

# Construction

The following chapter deals with the construction of the mechanical parts of the string. In the early stages of the development a 4t safe workload was specified for the strings, generously overestimating the maximum real load. All parts are designed for this workload.

### 7.1 Anchor

The anchor was designed by ONC with some modifications to the standard anchor design, as we required the ability to rotate the strings.

Two train wheels provide the main weight (625 kg weight in water). On top of these wheels a steel construction contains the connection points to the string and holding plates for the underwater Teledyne ODI connectors. This construction can be rotated against the train wheels and locked into position by moving a pin through holes in two steel plates and thereby fixing their rotation relative to each other. Whereas the upper steel plate contains only one hole and a welded on tube for holding the locking pin, the number of holes in the lower plate defines the angular resolution of the turning mechanism. 15° have been deemed a good resolution (Fig. 7.1). With this setup the string can be rotated at the bottom by a remotely operated vehicle (ROV) which would not have the capacity for rotating the string including the anchor due to its limited lifting ability of about 100 kg.

During deployment this structure on the anchor is fixed with a locking pin to avoid the structure from rotating in an uncontrolled way. With the mooring lines on the seafloor, the ROV removes the locking pin and disengages the rotating plate from the train wheels. The angular adjustment is done by the ROV turning the strings by pulling on a tow with a monkey fist on the end. Once in position a second locking pin is pulled. This locking pin has so far held a third locking pin in a tube in the upper steel plate. Once unlocked, the third pin falls down, ideally through a hole in the lower plate, thus locking them together. As the two steel plates are not necessarily perfectly aligned, the ROV will slowly rotate the top plate until the third pin falls into position.

The rotating structure on the anchor is protected from corrosion by sacrificial anodes and a zinc-based paint. The mechanism is lubricated with Blue Goop from Swagelok, a lubricant which in ONCs experience performs well in underwater conditions.

The rotating top plate of the anchor contains, apart from the connection points to the string, two U-shaped plastic constructions. Into these the ROV inserts plates with the Teledyne ODI wet mate connectors (Fig. 7.2).

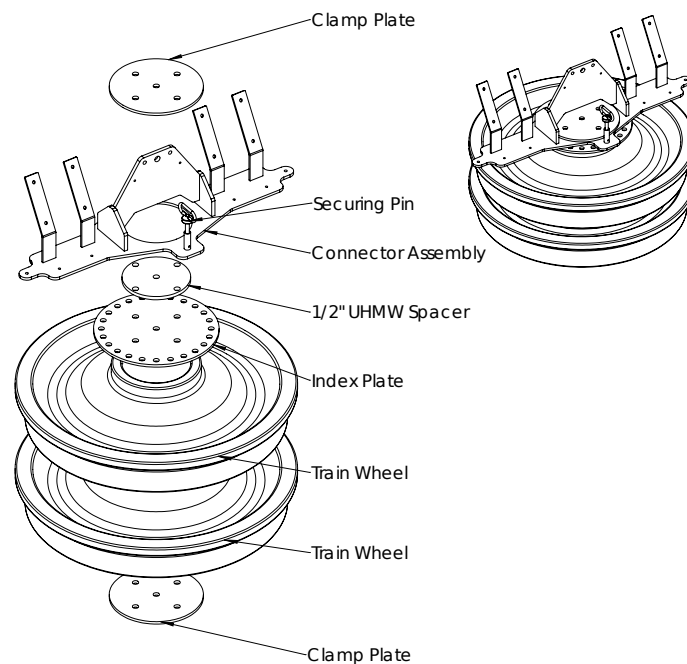


Figure 7.1: Anchor design by Dirk Brussow of ONC. The rotating structure is held together by threaded bars connecting the clamp plates. The two steel lines of a string connect to the Connector Assembly. The Connector Assembly part also provides two mounting points for two ODI connector plates.

For ROV operation the anchor is extensively marked, using color codes and arrows to show the desired orientation relative to the other string and junction box.

The connection between string and anchor is done using two interconnected shackles per wire rope. This allows a sharp bend of the string close to the anchor. If the wire rope were directly fixed to the anchor this bend would be limited to the minimal bending radius of the wire rope. The problem of this setup is that during deployment the string is towed behind the ship while the anchor is still standing on the deck, thus requiring a bend of more than  $90^\circ$  with the full pull of the string on it. To reduce the stress on the wire rope and allow an easier connection between string and anchor two shackles were inserted between between wire rope and anchor allowing for this sharp bend.

## 7.2 Module mountings

The module mountings were designed by Simon Hiller of ECP [Hil18]. The mountings provide the connection between modules and the string. Consisting of two steel plates kept apart by U-profiles, it uses custom milled clamps to fasten the data cables and DIN 1596 pipe clamps to fasten the wire ropes. On one side, where the module is attached, the steel plates extend to the module and have two elongated holes through which pipe clamps tie the modules to the mountings. Additional parts manufactured from polyoxymethylene

[Hil18] Simon Hiller. "STRAW: Entwicklung der Hardware Komponenten". MA thesis. Technical University of Munich, Aug. 2018



Figure 7.2: Anchor for the yellow string. The big yellow pin can lock the anchor into position. Two spare pins are tied to the anchor. The black U-shaped constructions serve as inserts for plates on which the data cables are mounted. Monkey fists on both sides of the anchor allow the ROV to grab and rotate. All pins are secured using cable ties that will break when the ROV pulls. Loops of rope are tied to each pin making it easier for the ROV to grab.

(POM) prevent the modules from slipping up or down. These POM parts have additional elongated holes so that a total of four pipe clamps can be used to fasten a module. All clamps were only used for the long and heavy SDOMs, for the POCAMs we used only two clamps. Before fastening, the titanium module housings were surrounded by Viton rubber. This and the POM parts ensured electrochemical separation of titanium and steel.

The one data cable connecting to the module performs a loop inside the mounting before connecting. This reduces lateral pull on the connector. The mountings were designed with cut-outs that would allow connecting and disconnecting of modules after the strings had been spooled on the winch.

SDOM and POCAM mountings were designed to use the exact same parts with the exception of two steel bars, that were shorter for the POCAM and longer for the SDOM.

### 7.3 Spacers

Along the length of a string several spacers keep the two wire ropes apart. The purpose of these spacers is first to hold the data cables, thus avoiding entangling and relieving the weight of the data cables from the module mountings, and second, to give some stiffness against twisting to the string.

The stiffness of the string is given by the fact that twisting the string would shorten it, thus dragging the buoyancy down. The lift of the buoyancy counters this and keeps the string straight.

To estimate the number of spacers needed for the necessary stiffness of the string, we first consider two wire ropes of length  $l$  kept apart at the top by a spacer of length  $2r$  and at the bottom by a spacer of length  $2R$ . The stiffness of the wire rope is neglected. Fig. 7.3.

shows a sketch of this setup. Without twisting the distance between the spacers follows  $h = \sqrt{l^2 - (r - R)^2}$ . If the top spacer is twisted against the bottom spacer this distance is reduced to:

$$h = \sqrt{l^2 - r^2 - R^2 + 2rR \cos \phi} \quad (7.1)$$

The potential energy to a buoy of lift  $B$  attached to the upper spacer is given by

$$U = B \cdot h \quad (7.2)$$

from which we can calculate the force  $F$  resisting the twisting of the upper spacer:

$$F = \frac{dU}{d(r\phi)} = \frac{B}{r} \frac{d}{d\phi} (l^2 - r^2 - R^2 + 2rR \cos \phi)^{\frac{1}{2}} = -\frac{BR \sin \phi}{h} \approx -\frac{BR \sin \phi}{l} \quad (7.3)$$

which means we have for a twisting angle  $\phi$  a torque  $M(\phi)$  of

$$M(\phi) = -\frac{BrR \sin \phi}{l} \quad (7.4)$$

especially for two spacers of same length  $r = R$

$$M(\phi) = -\frac{Br^2 \sin \phi}{l} \quad (7.5)$$

If we now introduce additional spacers, thus splitting the string into segments of length  $\frac{l}{n-1}$  each twisted by  $\frac{\phi}{n-1}$ , with  $n$  the number of spacers, we get

$$M(\phi, n) = -\frac{Br^2(n-1) \sin \frac{\phi}{n-1}}{l} \quad (7.6)$$

This formula holds as long as  $l \gg r$  and the twist of one segment has not reached  $\frac{\phi}{n-1} = 180^\circ$ . Once  $180^\circ$  has been reached, the two wire ropes will touch in the middle, effectively introducing a new spacer of length zero. The torque will drop significantly and, in the worst case, the string, having no more stiffness at that point, is now always aligning itself to the current.

We see now that a twist of  $180^\circ$  has to be avoided. From the optical point of view, ensuring that a clear line of sight is established between the modules of the two strings, the twisting angle should be a great deal smaller.

Estimating the torque created by a module of cylindrical shape and an effective area of  $A = 0.5 \text{ m} \cdot 0.2 \text{ m} = 0.1 \text{ m}^2$  we get for a water current at Cascadia Basin of  $v = 0.1 \text{ ms}^{-1}$

$$M_{\text{module}} = 0.6v^2 A \rho = 0.6 \cdot (0.1 \text{ ms}^{-1})^2 \cdot 0.1 \text{ m}^2 \cdot 1000 \text{ kg m}^{-3} \cdot r = 0.6 \text{ N} \cdot r_{\text{module}} \quad (7.7)$$

The modules have a distance from the string of about 10cm, thus

$$M_{\text{module}} = 0.6 \text{ N} \cdot 0.3 \text{ m} = 0.18 \text{ Nm} \quad (7.8)$$

A program was written to calculate the twisting of the string taking into account the heights of the modules and the weight of the string counteracting the buoyancy. The results showed that a spacer or mounting every 4-5m was sufficient, which means about 22 spacers per string (18 real spacers and 4 module mountings). Here we do a quick

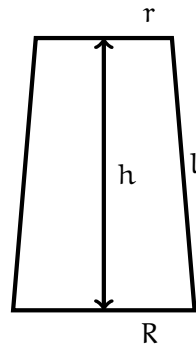


Figure 7.3: Sketch of two wire ropes of length  $l$  kept apart by spacers of length  $2r$  and  $2R$  at a distance  $h$ . If (in three dimensions)  $r$  and  $R$  are twisted against each other around the axis  $h$  by an angle of  $\phi$  we get  $l = \sqrt{h^2 + r^2 + R^2 - 2rR \cos \phi}$ , or, since  $l$  is fixed and  $h$  is of concern,  $h = \sqrt{l^2 - r^2 - R^2 + 2rR \cos \phi}$ .

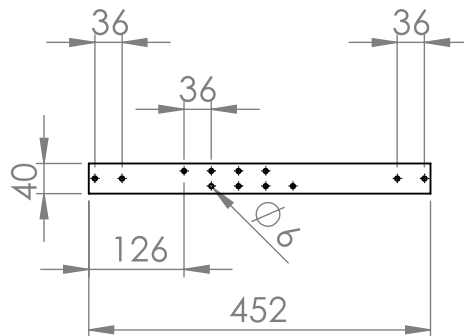


Figure 7.4: The spacer, keeping the wire ropes at a 400 mm distance, is a simple piece of 4 mm flat steel with holes to which DIN 1597 pipe clamps are bolted. All dimensions in millimeter.

estimate to check this value, simplifying the problem by assuming the torque of all four modules would act at the height of the highest module ( $l = 110\text{ m}$ ) and  $B = 1500\text{ N}$  being constant at all over the string, based on a buoyancy of 450 kg and a string weight of 300 kg. This will significantly overestimate the twisting angle  $\phi$ . Solving for  $\phi$  we get

$$M(\phi, 22) = 4 \cdot M_{\text{module}} \Rightarrow \phi \approx 76^\circ \tag{7.9}$$

which is the total twist of the string at 110 m and a sufficiently small value.

The spacers are simple 450x40x4 mm bars of steel with clamps for the wire rope and data cables bolted to them (Fig. 7.4). As clamps we used DIN 1597 pipe clamps.

## 7.4 Top spacer

The topmost spacer provides the connection point for the two thinner wire ropes, on which the other spacers and module mountings are fastened, and the thicker 30 m wire rope connecting to the buoy. For the thinner wire ropes, which have a threaded fitting



Figure 7.5: Top spacer. Two blocks of steel provide connection for the threaded fittings of the two thinner steel wire ropes. A 24mm bolt provides connection for the closed fitting of the thicker wire rope for the buoy. The M16 bolts holding everything together are still missing in this picture.

---

at the top end, it has two blocks of steel with through-going holes, against which the threaded fittings can be fastened with a nut at the top and another at the bottom. These two steel blocks are connected with two steel plates designed to withstand the 4t working load. A 24mm bolt goes through both steel plates and the fitting of the thicker wire rope. The steel blocks are bolted to the steel plates with four M16 bolts each (Fig. 7.5,7.6).

## 7.5 Compensating anchor tilt

If the anchor should sink unevenly into the sea floor and therefore tilt, we can compensate this by changing the wire rope spacing. The wire ropes have a distance of 40 cm at the bottom spacer, but only 10 cm at the anchor. This provides a reduction of the anchor tilt, the bottom spacer is tilted significantly less than the anchor. To maintain the same twisting resistance as the rest of the string, the bottom spacer is placed only 1 m above the anchor.

## 7.6 Bottom spacer

The bottom spacer provides a smooth transition between the 40 cm wire rope distance above and the 10 cm distance at the anchor. It consists of two steel plates, in which a rounded path for the wire rope was milled, thus avoiding a kink in the wire rope. The two steel plates are bolted together with M10 bolts and hold via friction onto the wire ropes (Fig. 7.7,7.8).

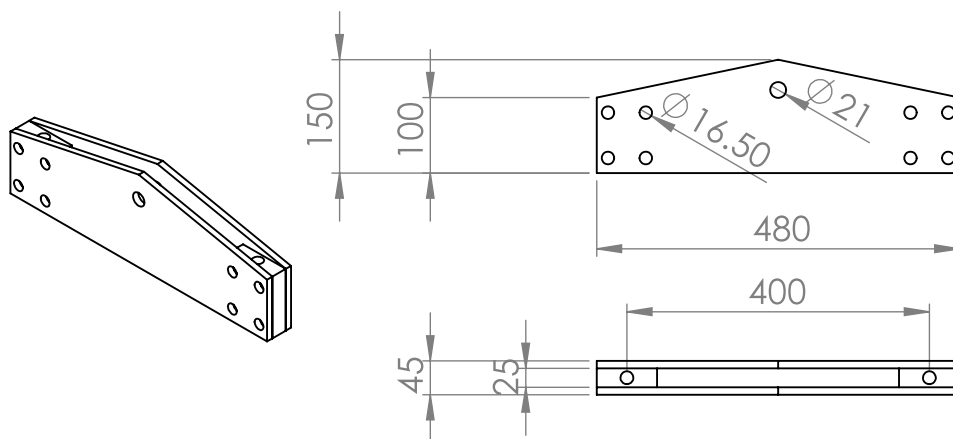


Figure 7.6: The top spacer provides a transition between the two thin wire ropes below, and the thick wire rope above. The thick wire rope has a closed fitting, by which it can be bolted to the spacer. The thin wire ropes have threaded fittings, they are fed through holes in two steel blocks and using nuts their length is adjusted. All dimensions in millimeter.

## 7.7 Mini junction box mounting

To provide mounting points for the mini junction box, the bottom spacer and the spacer right above it have additional holes, allowing to fasten the mini junction box with ropes and shackles.

## 7.8 Markings and nomenclature of strings and modules

To clearly distinguish the modules and strings the following scheme was chosen:

A string is identified by a color. Yellow and blue were chosen, as both colors are clearly distinguishable even under water, which is relevant for the ROV inspection after the deployment. The strings were therefore identified as string Blue and string Yellow. The winches for each string had clear color markings for distinction, equally markings were made on the anchors.

A module is identified by a number, SDOMs and POCAMs are numbered separately. For testing and post-deployment inspection adhesive labels were printed and stuck to the modules. The labels for the POCAMs show a number in a colored circle, the labels for the SDOMs show a number in a colored square; thus the modules can be identified even under bad optical conditions (Fig. 7.9).

To ensure module identification if the labels should come off, especially after the string recovery planned after two years of STRAW operation, the titanium housings were engraved with the same symbol as they show on the labels.

In the following chapters we will use the nomenclature explained above and refer to the strings as strings Blue and Yellow. String Yellow has two POCAMs and two SDOMs, thus, by having to light emitters, being the brighter string and having the brighter color. String Blue has one POCAM and three SDOMs.

For the underwater placement of the strings a similar mnemonic was used, string Yellow is east of string Blue, yellow corresponding to the rising sun.



Figure 7.7: Left: The steel plates for the two bottom spacers. Right: One assembled bottom spacer providing a smooth transition between a 40 cm distance and a 10 cm distance of the wire ropes.

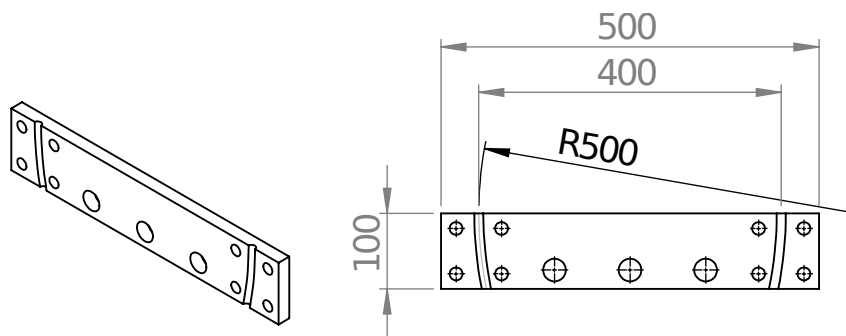


Figure 7.8: The bottom spacer provides a smooth transition between the 400 mm wire rope distance above and the 100 mm wire rope distance at the anchor. The bottom spacer consists of twice the drawn part bolted together. The wire rope runs in a smooth curve, which was milled into the steel. All dimensions in millimeter.

## 7.9 Steel wire rope

The steel wire rope was manufactured by Pfeifer of Memmingen. After consulting with the manufacturer we chose a 1x19 rope, meaning a rope consisting of one strand of 19 wires twisted together. Of the available options this was the one exerting the least twist when put under tension. Keeping up with the principle of having everything specified for a four ton workload, we went for two 130m PG-5 ropes forming the double string. These ropes have a limit tension of 3.6t. The single 30m wire rope connecting the top spacer to the buoyancy was a PG20 of the same type with a limit tension of 10.9t. The wires of the wire ropes were galvanized with GALFAN, a zinc aluminium alloy. The two thin ropes were additionally coated with black Lupolen (polyethylene) to reduce light reflection. Pressed onto the ends of the ropes were specific open and closed swaged fittings for easy connection to top spacer, buoy and anchor. Swivels by the same manufacturer were placed between the thick top steel rope and the buoy, thus ensuring that rotations of the buoy



Figure 7.9: Example labels for two modules. The module identification is clearly visible even for an underwater inspection. Additional information, e.g. the serial number, was added for storage and customs.

due to drag would not affect the string.

Pressed onto the top end of the thin coated ropes were threaded fittings. These fittings allowed the precise tuning of the string length, as it had to be ensured, that the two parallel wire ropes of each string have exactly the same length. The manufacturer was originally cautious concerning the precision of the machines cutting the rope to length, thus a long threaded fitting was chosen. During string assembly the parallel ropes were laid out, put under equal tension, and the final length was adjusted using nuts on the threaded fittings. The length deviation over 130m turned out to be only about 1 cm.

A disadvantage of the pressed fittings is their low tolerance of lateral stress. The very long threaded fittings therefore needed special care during handling.

## 7.10 Data cables

For the data cables connecting the modules to the mini junction boxes we followed ONCs experience and used Falmat Xtreme-Green cables. The used cables, purchased in black instead of the standard green color to reduce light reflections, had four single wires and four twisted pair wires, surrounded by Kevlar (polyaramid) fibers and a plastic coating. On the module side Subconn MCIL12M titanium connectors were molded to the cable as we had made good experience with these connectors with the POCAM prototype for lake Baikal and they were the preferred solution of the company doing the molding. On the mini junction box side Seacon GREXSL-12-CCP were used, as these were the preferred connectors of ONC.

Each module was connected by its own cable to reduce the risk of failure.

For the SDOM the four twisted pairs were used for RS-232, Ethernet and a synchronisation signal. The single wires were used for power, synchronisation ground and RS-232 ground.

Experience from ONC showed, that the 100m limit that is specified in the CAT standards is limited to about 70m due to losses in the subsea connectors. This limited the position

of the highest SDOMs to 70 m.

For the POCAM, apart from power, only a RS-485 half-duplex connection was used, requiring one twisted pair plus ground. This connection does not have the 70 m limitation, thus the highest POCAMs could be positioned significantly higher at about 110 m.

Of all parts of the string the cables were the most vulnerable. To ensure that abrasion and chafing during transport had not damaged them they were repeatedly tested for faults and electric connectivity.

## 7.11 Buoyancy

The buoyancies fastened at the top of each string have the purpose of keeping the string sufficiently straight in the current, so that the changes in displacement and orientation of the modules have a negligible effect on the measurements. As the simulations have shown, this can be done by a buoy with about 500 kg uplift.

An additional requirement to the buoy are two fastening points, one for the string at the bottom and another for the heavy lift line of the deployment vessel at the top. The shape of the buoy is of no particular concern.

After an investigation into the products of various buoyancy manufacturers a standard spherical buoy by DeepWater Buoyancy was chosen, as it fitted our requirements at the lowest cost and Ocean Networks Canada had good experience with the manufacturer.

The 51" Hydro-Float Mooring Buoy is a spherical syntactic foam mold with a polyurethane cover (Fig. 7.10). Connection points are provided by eye nuts at the poles of the sphere connected by a stainless steel rod. The composition of the syntactic foam changes with depth rating. The next higher standard depth rating for our 2600m site was 3500m, at which the 51" buoy has an uplift of  $450 \pm 38$  kg and a weight in air of 726 kg. While this uplift is slightly lower than the ideal 500 kg, the simulation showed that it was still a feasible value. Using a custom made foam composition for our depth, as was offered by DeepWater Buoyancy, was therefore not necessary. After manufacturing DeepWater buoyancy measured the precise uplift (seawater buoyancy) of both buoyancies at 446 kg.

As the color of the polyurethane coating is fixed to a standard orange used for many buoyancies, we chose to reduce unwanted light reflections by moving the buoy away from the top POCAM. After the top POCAM the top spacer connects the two wire ropes of each string. From the top spacer a 30m single wire rope connects to the buoy. This setup provides an easier and more reliable alternative to painting the buoy.

To simplify logistics and storage, the manufacturers sent the buoys not to TUM but directly to Ocean Networks Canada. ONC replaced the stainless steel eye nuts and rods with galvanized steel for galvanic compatibility with the rest of our strings.

Using additional buoys in the middle of our strings was considered. These cable floats can be clamped or bolted to a mooring line and are a common practise for bottom-up deployments, as they reduce the risk of entangling. With our top-down deployment they are not needed and would be counterproductive to the strings straightness, as they would reduce the string tension between themselves and the spherical buoy at the top, which would result in larger string tilt and twist. By mounting them only to the single wire rope at the top, this would not pose a problem, since no modules would be above them. This option was kept open in case the string would become too heavy, but was ultimately not necessary.



Figure 7.10: One of the 51” Hydro-Float Mooring Buoys in the ONC yard.

---

## 7.12 Transport

Due to the time constraints of the STRAW project the transport was split. The winches with the strings spooled onto them but the modules not attached were shipped via sea freight to Canada. The modules were shipped later via air freight. This gave us longer development time for the modules and an economic prize for the heavy strings and winches.

For the modules transport boxes with custom made foam inlays were used. The winches were directly screwed to the bottom of a custom wooden crate. In this setup no padding was necessary. For additional corrosion protection during transport the winches were wrapped in foil and dry packs were added (Fig. 7.11).

The buoyancies were shipped directly from the manufacturer in the USA to ONC in Canada.



Figure 7.11: Winches and modules being prepared for transport. The winches were send first via sea freight, the modules later via air freight, with the same estimated arrival time for both. Left: the winches were wrapped in foil for moisture protection and shipped in large wooden crates. Right: The modules had to be protected from mechanical stress and were shipped in padded cases.

---

## Chapter 8

# Calibration and testing

### 8.1 Measuring the data cable length

To get an absolute time stamp for each event, the runtime of the synchronization signal through the data cables had to be measured. For this the Medusa boards described in Section 5.3 were used. One was set up as master, sending a synchronisation signal, the second as slave, repeating a received signal. By connecting one at each end of a data cable to a twisted wire pair we could grab with an oscilloscope the time difference between the output signal in the master and the output signal in the slave. The same measurement was done with the cable that would later connect both mini junction boxes. From each measurement the time difference for a measurement without a cable (length zero) with only oscilloscope cables and adapters from Medusa to the data cables was subtracted. An overview is given in the following table:

cable to module	run time $t$	cable length $l$
SDOM3	200 ns $\pm$ 10 ns	35 m
SDOM4	200 ns $\pm$ 5 ns	35 m
SDOM2	315 ns $\pm$ 5 ns	56 m
POCAM2	315 ns $\pm$ 5 ns	56 m
SDOM1	420 ns $\pm$ 5 ns	75 m
SDOM5	420 ns $\pm$ 5 ns	75 m
POCAM1	650 ns $\pm$ 10 ns	117 m
POCAM3	650 ns $\pm$ 10 ns	117 m
ODI MJB to MJB	440 ns $\pm$ 10 ns	70 m

### 8.2 Magnetometer

Each module was equipped with an integrated 3-axis magnetometer and 3-axis accelerometer, that can be accessed over an I2C interface. A commercial chip designed for smartphones was chosen. The purpose of this chip is to give detailed tilt and orientation information about each module, allowing in the first stage to verify that the estimates about the string behaviour in the current done prior to deployment were acceptable and that the string is not entangled. At a later stage the data will allow us to get more precise optical measurements, as the angle of the modules relative to each other can be gathered

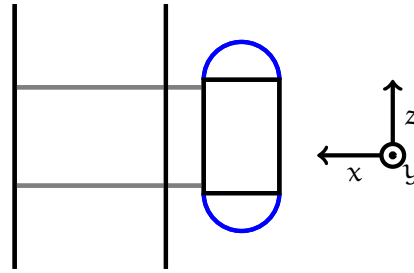


Figure 8.1: The module coordinate system for magnetometer and accelerometer measurements.

from it.

In principle the accelerometer measurements did not need any calibration. With a known orientation of the accelerometer inside the module the tilt can be calculated using simple vector geometry. The magnetometer on the other hand needs to be calibrated, as the magnetic field of the Earth is easily disturbed when large amounts of metal are nearby. This is especially the case for any magnetometer in a metal housing. In our case the titanium cylinder of the module housing disturbs the magnetic field and requires us to precisely calibrate the magnetometer.

The common solution for this problem is to assume a linear relation between measured and real magnetic field [KS16].

$$\vec{B}_{\text{real}} = M \cdot \vec{B}_{\text{measured}} + \vec{v} \quad (8.1)$$

An easy interpretation of this formula is as follows: the housing scales the magnetic field differently for different directions and adds its own field vector  $\vec{v}$ . The matrix  $M$  may also contain a rotational matrix, taking into account the orientation of the sensor inside the housing.

While it would be possible to measure  $\vec{B}_{\text{measured}}$  in  $n$  linearly independent orientations of the module,  $n$  being the degrees of freedom of the above formula, this would require precise knowledge of  $\vec{B}_{\text{real}}$  and precise positioning of the modules in the desired orientations. For ease of measurement a different approach was chosen.

A module was put into a continuous measuring mode, streaming magnetometer data to a computer many times per second. Then the module was, by hand and without high precision, rotated in air. For this the module was held upright, connector facing north, and then, around each of the three axis given by the coordinate system up-north-east rotated by more than  $360^\circ$  (about  $450^\circ$ ) and back. At the same time the accelerometer was also constantly taking data.

When plotting the data from the magnetometer (Fig. 8.2), one sees, after following this procedure, sine waves of varying amplitude in each component of  $\vec{B}_{\text{measured}}$ . Each of those waves has an offset, given by  $\vec{v}$ , that is constant over the entire measurement, and a specific amplitude depending on the axis of rotation. From offset and amplitude the magnetometer can be calibrated, a reasonably precise calibration is obtained just by visually analyzing the data, estimating amplitude and mean value (=offset) of each sine

[KS16] M. Kok and T. B. Schön. “Magnetometer calibration using inertial sensors”. In: *IEEE Sensors Journal*, Volume 16, Issue 14, Pages 5679–5689 (2016)

oscillation; a more precise calibration can be done using the accelerometer data taken at the same time.

The advantages of this method are, firstly, that it does not require additional equipment and therefore easily allows a recalibration at a later stage, e.g. if changes to the module would have been made in Canada; secondly, that only the direction of the magnetic field of the earth needs to be known and not the absolute value, being obtainable by a compass; and lastly that it provides an inbuilt sanity check. If the data should not show sine waves, some magnetic disturbance has occurred. While this did not happen during the final calibration of the modules, it happened multiple times during the development of the magnetometer driver, when measured data seemed to be self-contradictory, and it was later found out, that a nearby power cable or the steel enforcing of the lab desk had caused the problem.

It was considered to measure all modules at once, while on the winch. This approach had to be discarded as the large amount of steel used for the winch made magnetic measurements in its proximity almost impossible.

### 8.3 Vibration testing

During the deployment the STRAW strings were for several hours subject to a strong drag caused by seawater currents and their own descend velocity. As this drag can cause the string to vibrate, the modules were subjected to a vibration test. The test also helped us to estimate the effect of vibrations during transport to the modules.

We chose a standard test for oil and gas sub-sea applications with the following parameters (ISO 13628-6):

For each spatial axis, a frequency sweep from 5 to 25 Hz at 2 mm Amplitude, then a sweep from 25 to 150 Hz at 5g. Once 150 Hz was reached the sweep was repeated backwards. The frequency change was kept at 1 octave per minute.

For each of the three spatial axes four 10g 11 ms half sine shock in each direction.

The shock tests were done at iABG in Ottobrunn.

Aluminium adapters for the modules were produced mimicking the module mountings and allowing two modules, one POCAM and one SDOM, to be bolted to the vibration table. Most parts of the module mountings were reused for these adapters in order to test them as well. Thus the modules connect to the same POM parts as were later used for the mountings and are clamped to the adapters using the same type of clamps. Before the test sensors were glued to the housing of each module, allowing us to do a resonance search prior to the actual vibration test. Both modules were tested simultaneously on the same vibration table (Fig. 8.3).

During the vibration test, especially during the backwards frequency sweep, several bolts loosened and fell out of their screw holes. These were the bolts holding together the POM parts. Also two of the four clamps holding the SDOM broke (Fig. 8.4). The SDOM was held by four clamps, two clamping it to POM parts, two others clamping it to the aluminium adapters. In the final mounting these two clamps would clamp the SDOM to steel parts of the mounting.

In order to compensate these shortcomings in the final design, the following variations were made. The bolts, that for the vibration test adapters were not fixated with Loctite would be fixated on the module mountings. It was already planned before the vibration test to secure all bolts this way, however, we did not consider it to be a relevant point

for these specific bolts and therefore skipped this step for the adapter in order to easily disassemble the adapter again. Additionally the elongated holes for the steel clamps were fabricated in the mounting with a less rounded edge, as the clamps broke during the vibration test at the point where they were chafing against the aluminium adapters. For the shock test following the vibration test the broken clamps were replaced and the bolts fastened again.

The resonance search showed no significant resonance in either module.

After the tests the modules were reopened and tested. The result was that the modules themselves were completely unaffected by the test and still working, especially the electronics, which was our primary concern before the test, survived without any problems.

## 8.4 Pressure testing

Under the supervision of F. Henningsen of ECP, the housing manufacturer, Nautilus, performed a pressure test on the SDOM housing, which was, due to its length, significantly weaker than the POCAM housing. In a pressure chamber the pressure was repeatedly ramped up to 376 bar, a factor 1.5 higher than the expected pressure at Cascadia Basin of 260 bar. The pressure was held for 15 min at its maximum value and then quickly ramped down. Additionally a 15 min test at 80 bar was done, to check the module housing at the low pressures.

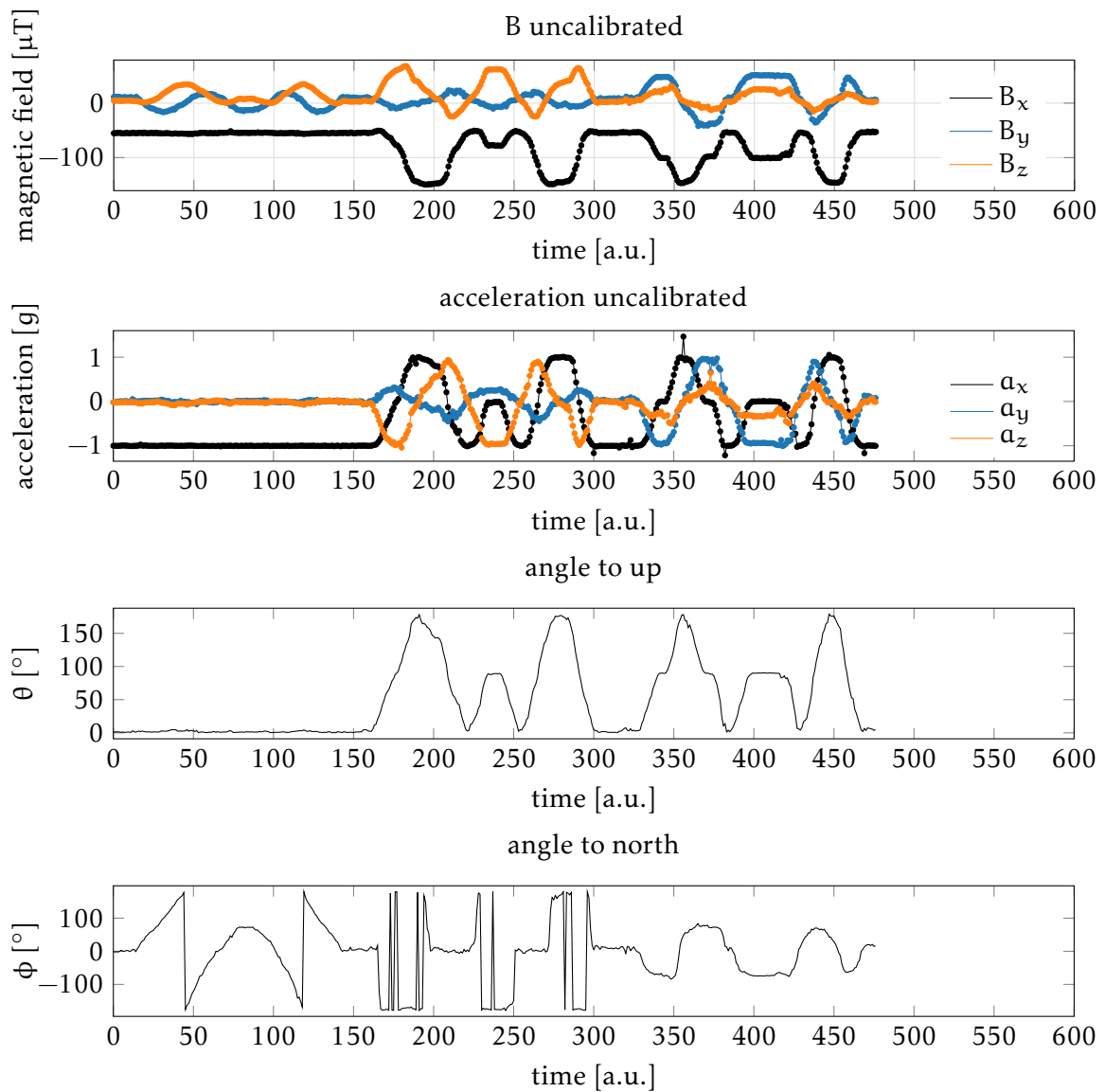


Figure 8.2: Top: uncalibrated magnetometer data from a calibration sweep during which the module was rotated by  $450^\circ$  and back around each of its axes, showing rough sine waves. Middle: accelerometer data from the same sweep. After removing the offset from the magnetometer data by centering the sine waves around zero and using the accelerometer data to gather the relative orientation between magnetometer and module, the calibrated magnetometer and accelerometer data can be calculated. Bottom:  $\theta$  and  $\phi$  angles of the module,  $\phi$  being the angle clockwise from north. The angles are calculated from the calibrated data, showing exactly orientation towards north at the beginning of the calibration run and then the rotation around each of its axes  $z$ ,  $y$  and  $x$ .



Figure 8.3: Setup of the two modules on the vibration table at iABG. The longer SDOM, held to the aluminium profiles acting as adapter to the table, is fastened using four clamps. The photomultiplier is covered by thick black tarp. Sensors on the modules (blue cables) allowed a resonance scan. Both modules were tested simultaneously.

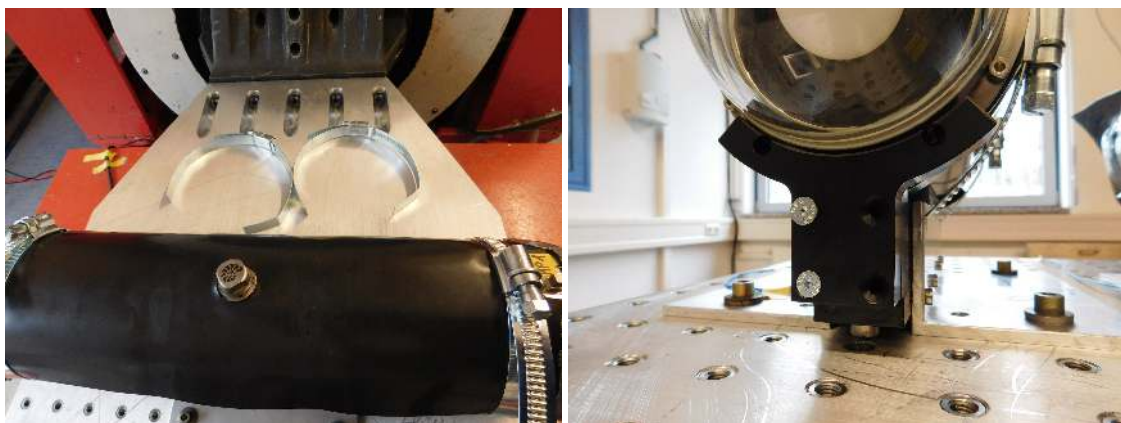


Figure 8.4: Left: SDOM on vibration table with two broken clamps and two clamps that survived the vibration testing. Right: POCAM on vibration table with two of the four bolts holding the POM parts together missing and one bolt partially unscrewed.

## Chapter 9

# Designing a winch for string deployment

For convenient deployment, testing and transport a winch was designed, capable of spooling and unspooling a string (Fig. 9.1). The string was spooled onto the winch at TUM and unspooled on the ship directly into the water.

### 9.1 Expected forces and dimensioning

A quick estimate showed that a winch capable of withstanding the forces of an anchor-first deployment would be too massive for convenient construction at TUM. Additionally this deployment style would greatly improve the stress on the strings themselves, therefore making possible entanglements more dangerous. A buoy-first deployment was chosen.

According to the deployment strategy the strings would be spooled consecutively into the water, the top end with the buoy being dragged away from the deployment vessel by a small rigid-hulled inflatable boat (RIB), thus preventing the string from entangling with itself. The forces acting on the winch were therefore hard to estimate, it was reasonable to assume that they would not exceed the total weight of the string, as ideally half of the string weight would be carried by the buoy and half by the winch. The additional forces created by the dragging RIB would be in the same order of magnitude. Estimating the string weight to 300 kg and the winch diameter to 50 cm, with a safety factor of 2 we get an expected torque of 3 kNm. All parts of the winch were designed according to this torque, the only exception being the motor, which, under the limitations of size and cost, could only provide a torque of 2.4 kNm. With the buoy-first deployment strategy the winch would not have to carry the weight of the anchor. After unspooling the entire string, the anchor would be fixed to the string end and the load transferred from the winch to the heavy lift line of the ship.

### 9.2 Material

The parts of the winch were made from S235JR steel, which according to [Hei+] has the following relevant parameters: a tensile strength under pull of  $\sigma = 150 \text{ Nmm}^{-2}$ , a tensile strength under bend of  $\sigma = 170 \text{ Nmm}^{-2}$  and a torsion strength of  $\tau = 120 \text{ Nmm}^{-2}$ . All

---

[Hei+] Max Heinzler et al. *Tabellenbuch Metall*. 40th ed. Europa Lehrmittel. ISBN: 978-3-8085-1727-7

the values are the strength under alternating stress, taking into account that the winch could operate with repeated jerks.

### 9.3 Motor

Each winch was powered by a motor with a gearbox and brakes by SEW Eurodrive. An important criterion was the ability of the motor to run with the power supplied by the deployment ship (460V, 60Hz, 3 Phases) and the power grid at TUM (380V, 50Hz, 3 Phases). The chosen motor and its control electronics fulfill this criterion, with a small change in rotational speed being accepted as a negligible side effect.

A bevel gearing with a transfer factor of 330 gives the motor a torque of 2440Nm at 60Hz while reducing the revolution speed to 5 revolutions per minute, corresponding to a speed of less than one meter per second for the string unspooling. This slow speed ensured that the operator of the winch could stop it in the case of problems.

Electronic controls also provided by SEW Eurodrive let the motor slowly ramp up to its maximum speed, and ramp down on switching off, preventing a sudden jolt of the winch due to its large mass being accelerated. A hand-device providing the basic functionality of powering on the motor, choosing revolution direction and emergency stopping was built by Christian Spannfellner of ECP. A second emergency stop button was placed at the side of the winch. The emergency stop bypasses the ramp down and brings the winch to a sudden halt, providing some safety to the personnel working close to it, as, even though slow, due to the large torque the winch can be extremely dangerous. The electronics were placed in a control cabinet next to the motor. Tests at the lab showed strong vibration of the control cabinet, which were then suppressed by rubber buffers.

### 9.4 Axle

The diameter of the axle is defined by its counterpart, the hollow axle of the motor. Following the industrial convention, a motor with a torque of around 2500Nm has a 60mm hollow axle. It would be custom to use a higher quality tool steel for an axle, such as C45, for ease of manufacturing and welding we nonetheless used the same S235JR construction steel that was used for all other steel parts, which was considered acceptable since the winch would do only few rotations during its lifespan. To manufacture the axle a 65mm rod was lathed down to 60mm where the motor and bearings would be mounted. Two steel plates were welded to the axle, providing a connection to the spokes. Standard ball bearings held the axle in place. Motor and axle were connected using a feather key.

The polar section modulus of a round axle is given by

$$W_p = \frac{\pi d^3}{16} = \frac{\pi \cdot (60\text{mm})^3}{16} = 42412\text{mm}^3 \quad (9.1)$$

with a torsional moment of

$$M_t \approx 2500\text{Nm} \quad (9.2)$$

we can calculate the torsional stress

$$\tau_t = \frac{M_t}{W_p} \approx \frac{2.5 \cdot 10^6 \text{Nmm}}{4.2 \cdot 10^4 \text{mm}^3} \approx 60\text{Nmm}^{-2} \quad (9.3)$$

which, with a resistance to alternating stress of  $120\text{Nmm}^{-2}$  of the material, is small enough. Additionally we have to take into account the bending moment caused by the weight of the wheel

$$M_v = \sqrt{M_b^2 + 0.75 \left( \frac{\sigma_b}{\phi \tau_t} M_f \right)^2} \quad (9.4)$$

where  $\phi$  is a factor describing the behaviour of the material (brittle/ductile,  $1 \leq \phi \leq 2$ ). We skip the precise calculation and estimate  $M_v \approx \sqrt{M_b^2 + M_t^2}$  and  $M_t \approx M_b$  for the bending moment caused by a 300 kg string on a one meter axle held at both ends. We see that  $M_v \approx \sqrt{2}M_t$  which can still be endured by a 60 mm axle.

## 9.5 Wheel

The wheel of the winch consists of eight pairs of spokes, interconnected in  $\phi$ -direction by flat-bar steel distributing the load to multiple spokes. In  $z$ -direction (parallel to the axle) the spokes were connected via larger parts of flat steel, on which the steel wire rope and the data cables would run. For the protection of the data cables, edge guards were mounted to these steel parts. Two small bars of steel, bolted to each of these parts, separate data cables from the steel ropes, with the data cables running in the middle and the steel ropes running at each side (Fig. 9.2,9.2). The spokes connect to two steel plates welded perpendicular to the axle. As with the 10 mm thickness of these plates the shearing stress between the plates and the axle is high, a feather key connection was not deemed sufficient. The connection is thus made by continuous welds. As the wheel consists only of four different parts, although in larger number, CNC laser cutting was used for the production of these parts. Due to time constraints no corrosion protection was applied. The metal cutouts for the spokes were bend to form 40x20x3 mm U-profiles. Using the section modulus  $W$  of a u-profile

$$W = \frac{BH^3 - bh^3}{6H} = \frac{25\text{mm} \cdot (40\text{mm})^3 - 22\text{mm} \cdot (34\text{mm})^3}{6 \cdot 40\text{mm}} = 3064\text{mm}^3 \quad (9.5)$$

where  $B$  and  $H$  are the outer,  $b$  and  $h$  the inner measurements of the profile, we can calculate the acceptable torque  $M$ . Like all other parts the spokes were manufactured from S235JR.

$$M = \sigma W = 170\text{Nmm}^{-2} \cdot 3064\text{mm}^3 = 521\text{Nm} \quad (9.6)$$

This shows that the maximum torque has to be distributed to six spokes, or three spoke pairs, which is ensured by connections between the spokes made from 20x2 mm flat steel. These pieces withstand a pulling force of  $F = \sigma A = 150\text{Nmm}^{-2} \cdot 40\text{mm}^2 = 6\text{kN}$ , which, being bolted to the spoke in the middle, corresponds to 3 kN applied at the end of the spoke, which is our maximum load. Following the instructions for bolt dimensioning from Würth [Wür] M10 bolts were used for the entire wheel. Using specifically tailored

[Wür] Würth. *Dimensionierung von metrischen Schraubenverbindungen*. [https://www.wuerth-industrie.com/web/media/de/pictures/wuerthindustrie/technikportal/dinokapitel/Kapitel\\_06\\_DINO\\_techn\\_Teil.pdf](https://www.wuerth-industrie.com/web/media/de/pictures/wuerthindustrie/technikportal/dinokapitel/Kapitel_06_DINO_techn_Teil.pdf), retrieved on 10.10.18

bolts for the various expected forces was disregarded in favor of having only one type of bolts, thus simplifying construction and maintenance.

The separation of data cables and wire ropes on the winch was a necessary step to ensure that under tension the wire ropes would not cut into the data cables. It had to be ensured that the bulk of the data cables did not grow faster in diameter than the bulk of the wire ropes. Otherwise the spacers would bend over the data cables, possibly damaging them. The wheel of the winch was separated by small steel bars into three compartments, wire ropes at either side and data cables in the middle. The middle compartment was significantly wider, thus ensuring that the bulk of the data cables would grow only slowly in diameter.

## 9.6 Frame

Following [Wür] M16 bolts were considered sufficient for all connections of the frame. The frame consists of 100x100x4mm square steel pipes held together by 10mm steel plates in the corners. The steel plates on the floor of the frame have bolt holes, wooden blocks were bolted to them as feet of the winch. The dimensions of the frame match a Euro-pallet for easy transport with forklifts. Two steel plates at the top of the frame provide hoist points (Fig. 9.4) .

## 9.7 String assembly and spooling

In the following paragraphs we will refer only to one string. All steps were the same for the other string.

For the assembly of the strings a 200m long room at TUM was used (Fig. 9.7). First the wire ropes were stretched out and put under tension. Bottom spacers and top spacers were mounted and, using the threaded fittings on the ends, all wire ropes were set to the same length. Markings were made on the wire ropes at given distances. Using these markings we could ensure that the spacers were mounted parallel and determine their exact position on the string. Now the spacers and mountings were assembled onto the strings at their intended positions, with the bolts not tightened yet, allowing further adjustments. The strings were assembled on carpets, thus allowing them to slide over the floor when the winch was put into action.

Alongside the string the data cables were laid out and tested for faults.

From the bottom spacer three 5 m ropes were tied to the axle of the winch. Therefore the first turn of the winch would be rope, which can be cut on the ship to release the string (Fig. 9.5). Three ropes were used, as one central rope would bear the load and be cut last with two other ropes as backup. By using a rope tied to the center of the bottom spacer a skew of the bottom spacer could be avoided.

Then the ends of the data cables, which would later connect to the mini junction box at the bottom of the string, were led into the frame of the wheel and out on the side. Here they were zip-tied to the wheel in a loop. By leading the data cable ends through the interior of the wheel we allowed access even after the entire string had been spooled on top of them.

The winch was then slowly operated, spooling the string. When necessary, string tension was provided by pulling the end of the string by hand. Shortly before a spacer would land on the winch, its position would be adjusted, making sure that it fitted between the

spokes of the winch wheel and not jam during unspooling. Then the bolts on the spacer were tightened, locking its position (Fig. 9.6).

During the spooling it was ensured that the data cables were always slightly longer than the wire ropes. This slack ensured that the load would never be carried by the data cables. While it was relatively easy to sort the wire ropes on the winch to neat bundles, the data cables caused problems due to their slack, bulging and not lying flat.

We found that the best solution to the spooling was having two people to either side of the string slowly guiding it onto the winch and providing some tension in the rope, while a third person would sort the cables on the winch to flat bundles (Fig. 9.6).

When mountings were fixed to the string their position needed larger adjustment than the spacer position, as we had to distribute the mountings equally around the wheel, with  $90^\circ$  between them guaranteeing sufficient space for the modules. Based on the distance markings on the string, the final positions of the module mountings was written down for later data analysis.

It is therefore important to understand that using the winch for deployment the position of the modules can not be fixed in advance, but needs to be adjusted during spooling, which can shift the module position by up to 2 m.

After the string had been spooled, it was unspooled again. This tested the winches and the spooling concept, and showed that unlike spooling, which took several hours, the unspooling took, as planned, about 20 minutes and required, apart from controlling the motor and carefully guiding the mountings to the floor, no further intervention. We simulated the behaviour of the buoy being dragged behind the ship by pulling the top of the string by hand, thus stretching it out on the carpet again. Now a last check was made on the spacers and mountings. A vital step at this point was to check the data cable slack again, as due to the bulging of the data cables on the winch the slack could not always be estimated. Some adjustments were made and the strings were spooled again.

In order to allow the deck crew to estimate the process of the unspooling each spacer had been marked with a number counting down. Before the bottom spacer a red warning sign was tied to the string signalling that the end of the string was imminent.

After the second spooling, the spools were prepared for transport. Using zip ties the wire ropes and data cables were tied to the winch so that they would not change their position during transport and handling.

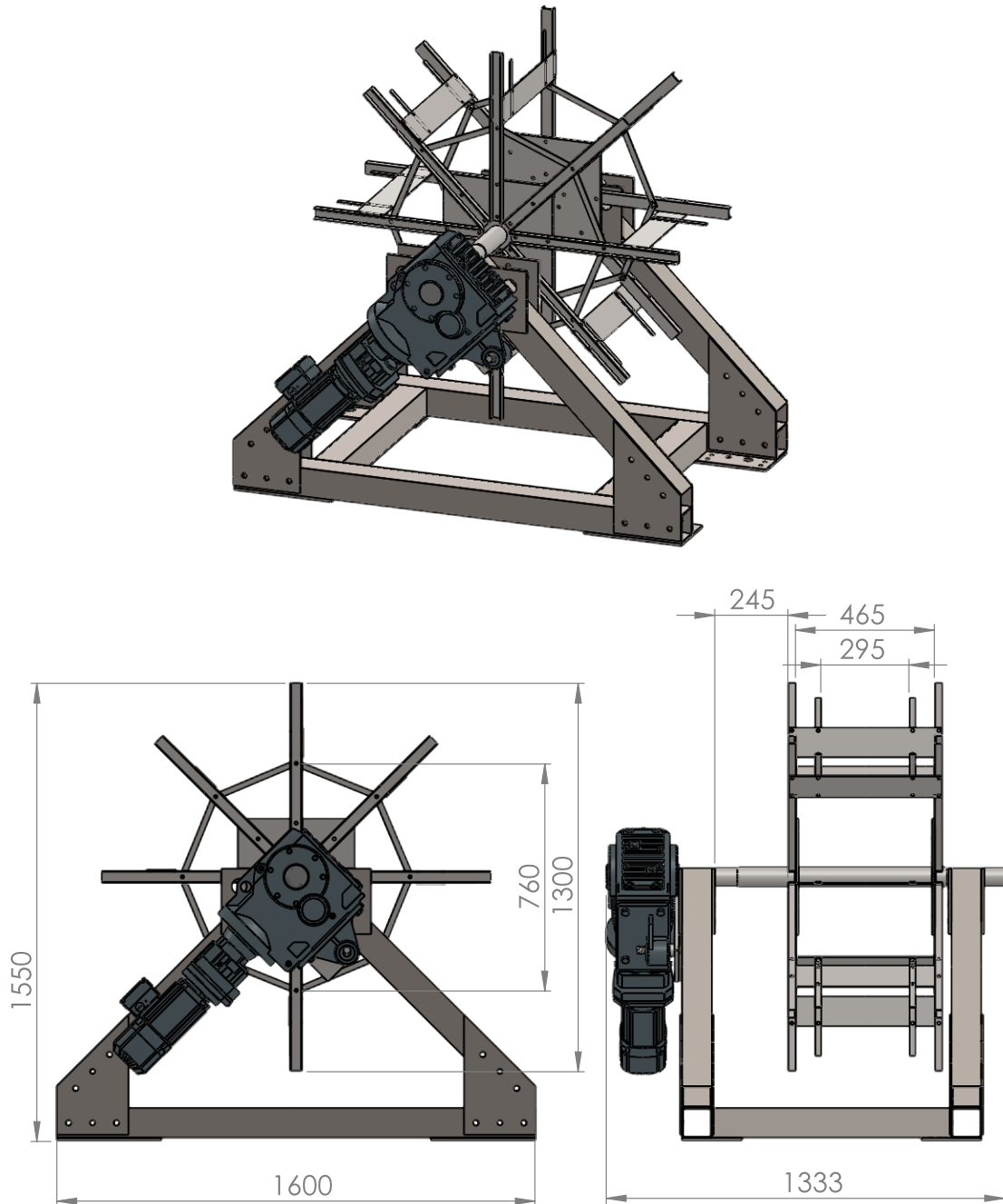


Figure 9.1: The winch developed for convenient string transport and deployment. An integrated system of motor, gear and brakes moves a wheel, on which the string is spooled. The modules extend over the side of the wheel and can rotate in a free space between wheel and motor.

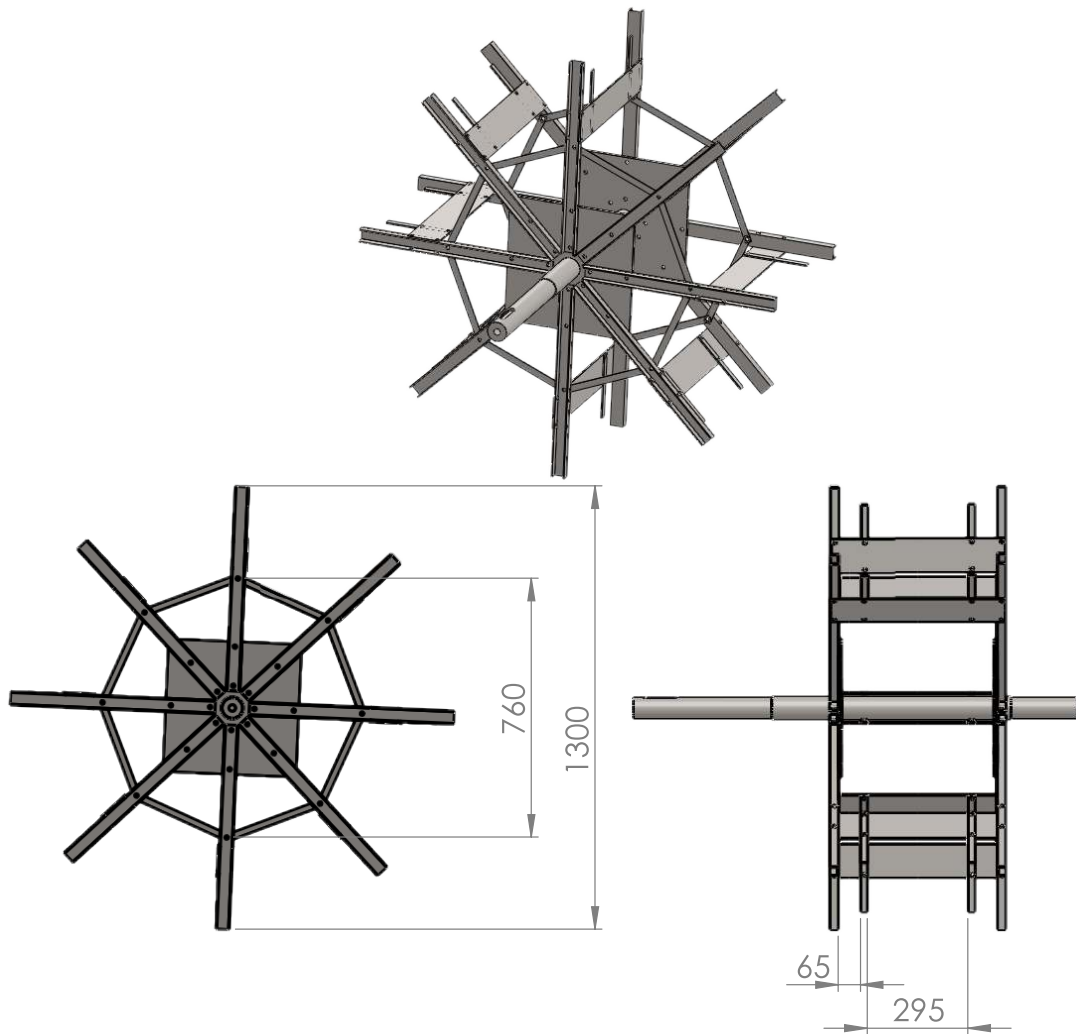


Figure 9.2: The wheel of the winch. In three compartments the two wire ropes and the data cables are stored. The modules extend over the side of the wheel. During spooling it has to be guaranteed that the spacers and mountings always land between the spokes.



Figure 9.3: Winch with motor and wheel assembled under a crane at TUM.



Figure 9.4: Left: The frame of the winch without motor and wheel. Wooden blocks were used as feet. Right: The frame of the winch with the axle in the ECP office. Welded to the axle are the connection plates for the spokes. The axle is held by industrial ball bearings. The hot-dip galvanized connection plate provides hoist points.



Figure 9.5: The first turns on the winch were made with ordinary rope which is tied to the bottom spacer. During deployment the string will be disconnected from the winch by cutting the ropes. The ends of the data cables lead out of the interior of the winch wheel for testing purposes. Later they were rolled up and tied to the side of the winch wheel.

---

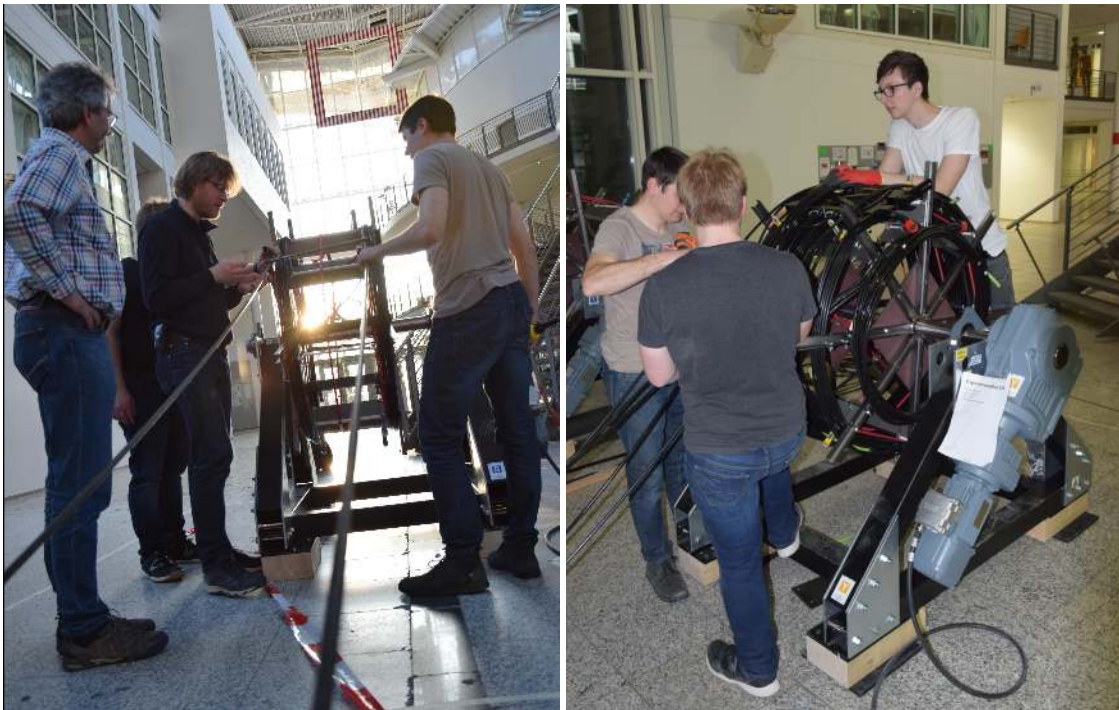


Figure 9.6: Left: Spacers are mounted shortly before they are rolled onto the winch, thus making sure that they fit between the spokes. Data cables are fixed with a little slack, ensuring that the load is always on the steel wires and never on the data cables. Right: S. Hiller and A. Gärtner mounting a spacer. F. Henningsen (right) sorts the data cables and steel wires on the winch to flat bundle. [Hen]

---



Figure 9.7: The 200m long building of the TUM Engineering Department was used for string assembly. The strings were laid out parallel to each other, mountings and spacers were attached, and the strings were spooled onto the winch. [Hen]

---

## Chapter 10

# Deployment preparation and testing at Ocean Networks Canada

As ONC requires extensive underwater testing before experiments can be deployed, several members of the STRAW team joined ONC in Victoria to prepare and test STRAW in May 2018.

The modules, which had been sent separate from the winch, were tested in a small salt water tank for electrical current losses (Fig. 10.2) and then mounted to the strings on the winches. Each module was then tested through its data cable on the winch.

The Medusa synchronisation boards were mounted into the mini junction boxes and tested (Fig. 10.1).

A demonstration of the unspooling procedure with the winches was made to the ONC personnel responsible for the deployment (Fig. 10.4).

After the string assembly, the winches were put into a large outside salt water tank and tested individually by ONC for several days .

The strings were then tested in combination with the mini junction boxes. During this testing a small problem with the synchronisation signal was observed which turned out to be caused by an unsteady power supply and could be fixed on site.

Once the synchronisation worked in the dry, both winches were put to a full integration test, connected in the same way as they would be in the sea, and submerged into the pool again (Fig. 10.3,10.4). During this test they were connected to the instrument platform, which was also submerged in the test pool. After the tests had been successfully passed, the winches were recovered from the pool, hosed down with sweet water and prepared for transport on the ship (Fig. 10.5).

During this time ONC made last modifications to our and their designs, making sure that the mini junction boxes and anchors provided by ONC would fit without problems. The deployment strategy, which had been outlined before, was finalized.



Figure 10.1: Left: interior of a mini junction box designed by ONC. The dry mate connectors leading to the modules are covered with red caps. Inside the mini junction box power converters, a network switch, a serial server, various relays and the Medusa board are mounted. Right: a closed mini junction box in a black anodized aluminium housing.



Figure 10.2: Left: Modules mounted on the winch for the first time at ONC. After mounting, the modules were tested through the data cables on the winch. Right: Test of a SDOM in a small water tank at ONC. The PMTs were protected from light by a plastic cap. ONC paid special care that the housing was not on the electric potential level of the power supply, as their fault protection would shut down a module if power and sea water were on the same potential level.

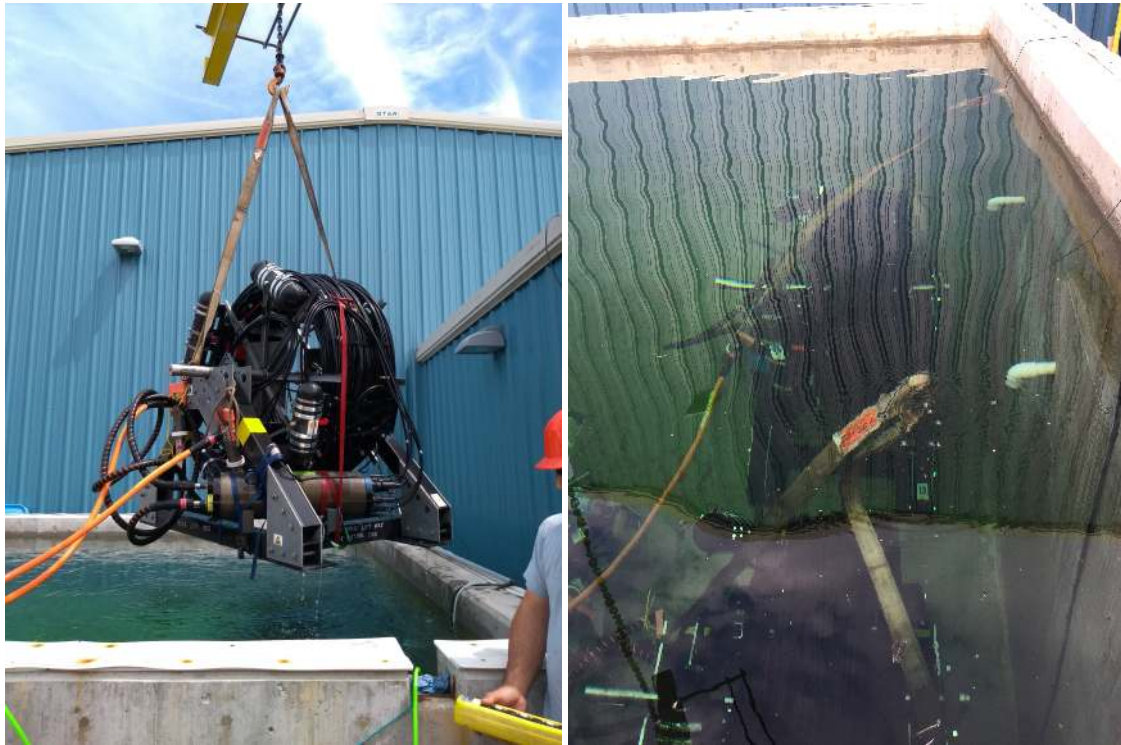


Figure 10.3: A winch shortly before and after being submerged in the large ONC test tank. During this test the strings on both winches were connected to the junction box, which was also submerged. Then the fully integrated system was run and tested over several days.

---



Figure 10.4: Left: As a concession to our light-sensitive photomultipliers, ONC covered the salt water tank with a large tarp during the prolonged testing. Right: Test first ten meters of the yellow spool were unspooled at ONC to demonstrate the operation of the winch to ONC personnel that would be on the deployment vessel.

---

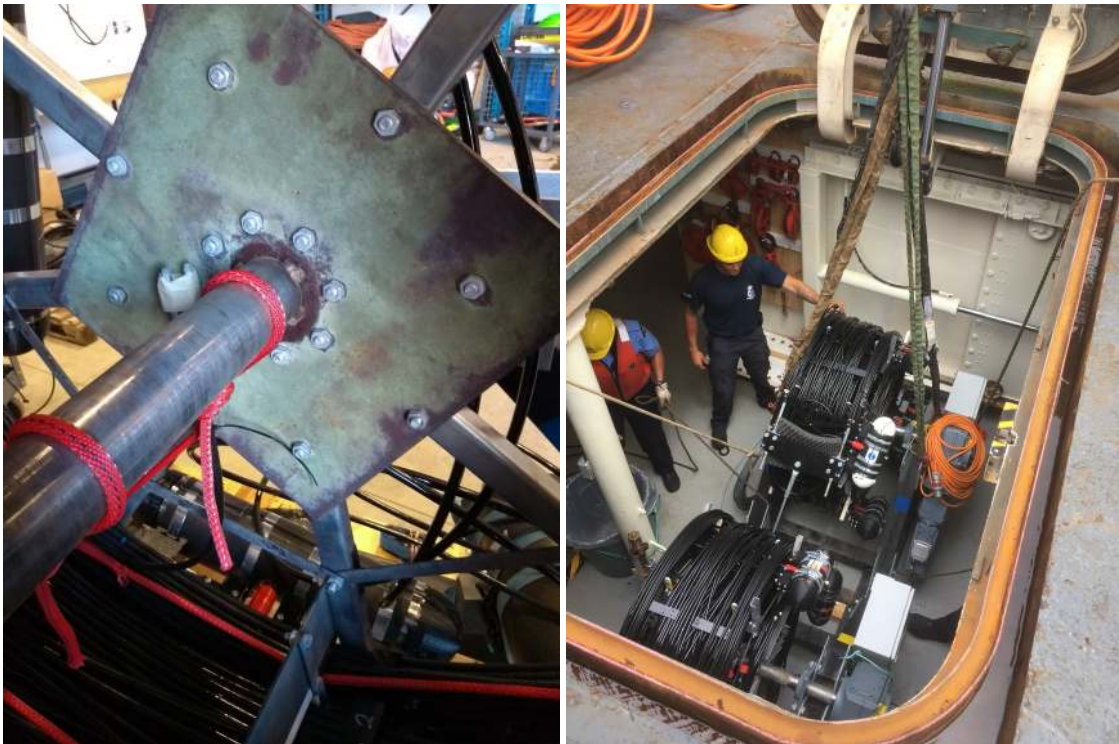


Figure 10.5: Left: Unprotected parts of a winch showing signs of corrosion after the test tank. Right: The two winches in the ships bay.

---

## Chapter 11

# Deployment

For a deployment of a mooring line two strategies are common, the bottom-up and the top-down deployment. For a bottom-up deployment the mooring line is compactly stored and deployed to the sea floor in this compact form. Then a release mechanism is triggered and the mooring line is pulled up by its buoy and unfolds. For a top-down deployment the mooring line is lowered in its extended form into the water and then lowered to the sea floor. The disadvantage of the top-down deployment is that the mooring line has to travel through the water in its extended and rather vulnerable form, the advantage is that no complex release mechanism is needed, and stages of the line assembly can be done on the ship right before the assembled part is submerged. We used a top-down deployment for STRAW.

A top-down deployment can be done in two ways, the anchor-first approach and the buoy-first approach. The anchor can be lowered into the water first, the mooring line therefore hangs almost vertically down and the full weight of the anchor is always pulling on the line. Alternatively, the buoy can be deployed first and is then dragged behind the ship. The buoy-first deployment requires a more complex procedure, as the buoy has to be brought back to the ship to connect it to the heavy lift line before the string can be submerged. Its advantage is that it puts significantly less stress on the string during the deck operations.

The deployment strategy, as worked out by Klaus Leismüller of ECP and Paul Macoun of ONC, was based on a buoy-first deployment. Based on weather forecasts a day with very low sea activity (sea state 1) was chosen for the deployment. As the buoyancy at the top of the string would not be able to keep string and anchor afloat, a second buoyancy was fastened to the string. While a winch was operated on the back deck of the CCGS John P. Tully, a RIB pulled away the top of the string (Fig. 11.1). The winches slowly unspooled the strings into the water, while ONC personnel guided the modules over the rear of the ship. After a string was completely unspooled its end was pulled back several meters onto the back deck and the mini junction box was mounted. Jeff Bosma of ONC performed a last functionality test on the strings, then the anchor was attached, lowered into the water and released (Fig. 11.2). The anchor was hereby carefully lowered several tens of meters into the water to prevent the string from acting like a pendulum. The RIB closed up with the Tully, the second buoy was removed and the top of the string connected to an acoustic release on the heavy lift line of the Tully. The string was then slowly lowered into the sea and, based on a depth measurements by an acoustic beacon, released few meters above the sea floor (Fig. 11.4). After both strings and the instrument platform, which had been deployed first, were on the sea floor, the ROPOS ROV was lowered into the water, made

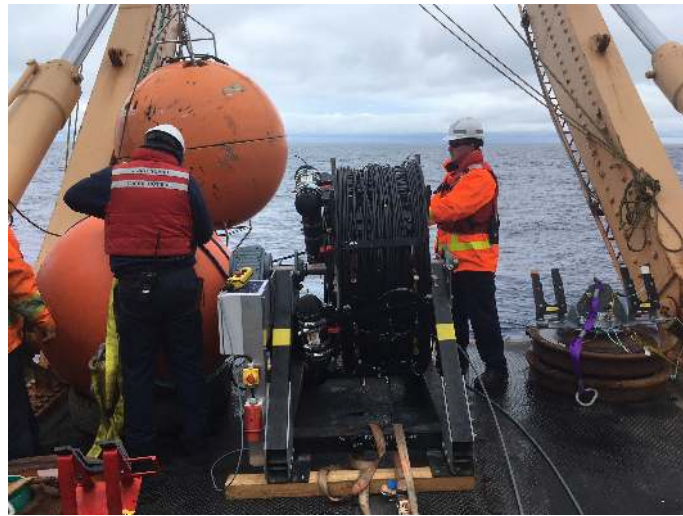


Figure 11.1: Unspooling of the yellow string from the back of the ship.

---

an optical inspection and, by lifting the strings from the top, made the fine positioning. The ROV then released the rotation mechanism of the anchors and rotated both strings in such a way that the modules faced each other (Fig. 11.5). Then the connections between mini junction boxes and the instrument platform were made. Afterwards the ROV flew along each string to allow ECP in Munich a last inspection of the strings under water (Fig. 11.3).

While the unspooling and testing was rather quick, the slow lowering to the sea floor, which was necessary to reduce the risk of entangling, prolonged these operations to more than one day.

After the deployment the strings were powered on and each module was tested and responding.

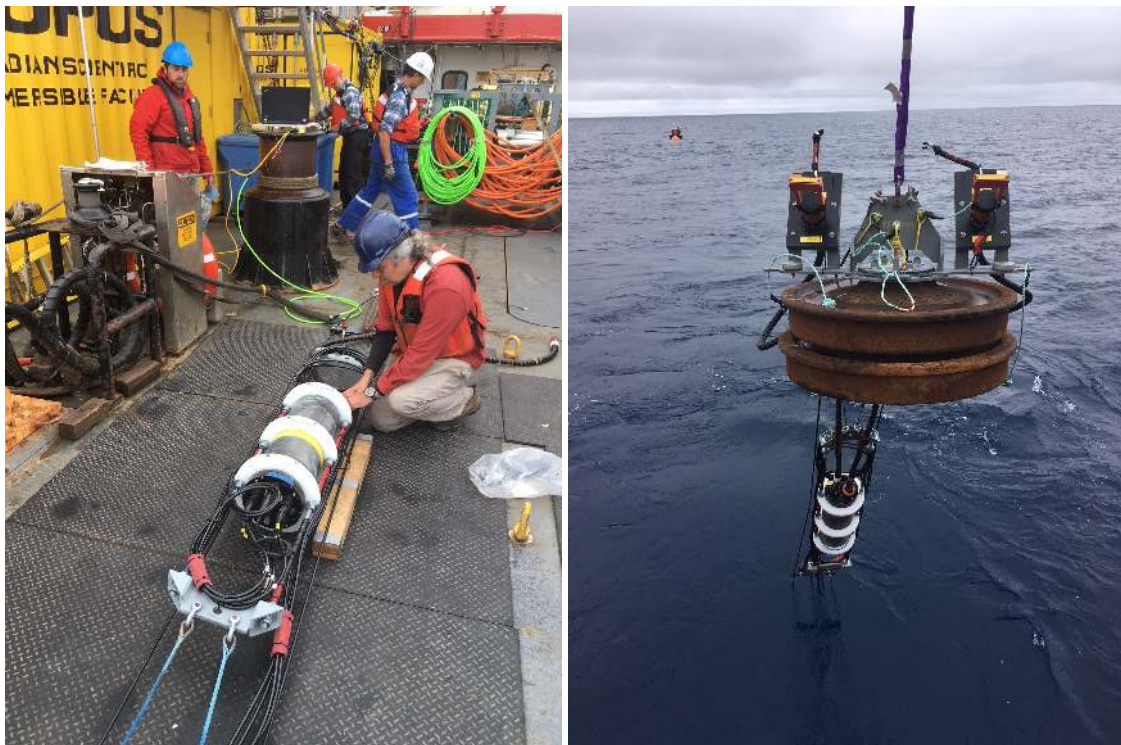


Figure 11.2: Left: After unspooling the end of the string was pulled back onto the deck to mount the mini junction box between the two last spacers. ONC then performed a last test, powering up all the modules in the water and establishing a short data connection. Right (near): The anchor is lifted into the water. The mini junction box is still above the surface. Right (far): The RIB is towing the buoy away from the ship, stretching out the string in the water.



Figure 11.3: Images from the string inspection by the ROV. Left: The top spacer which acts as a transition between the double wire rope, on which the modules are mounted, and the single wire rope, to which the buoy is fastened. Right: SDOM4 on the yellow string.

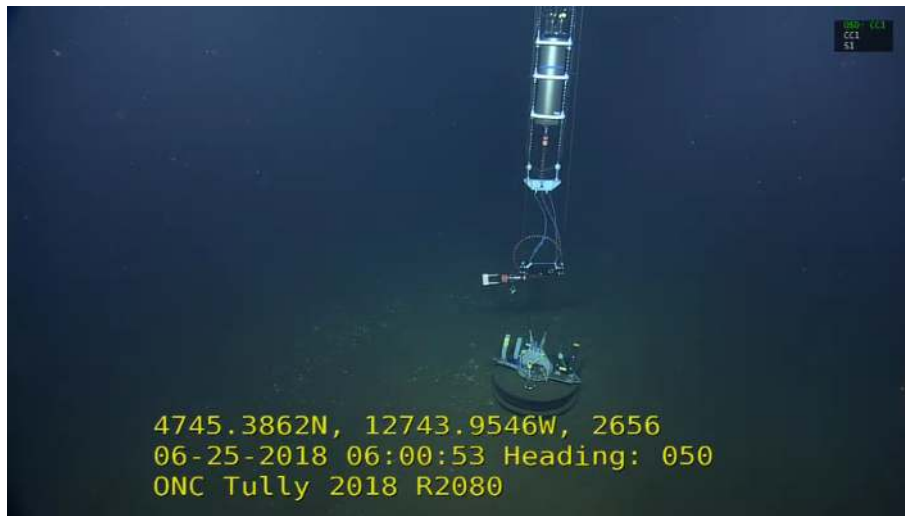


Figure 11.4: View of the anchor and the mini junction box on the sea floor. The anchor consists of two train wheels, one of which has sunken into the sea floor.

---

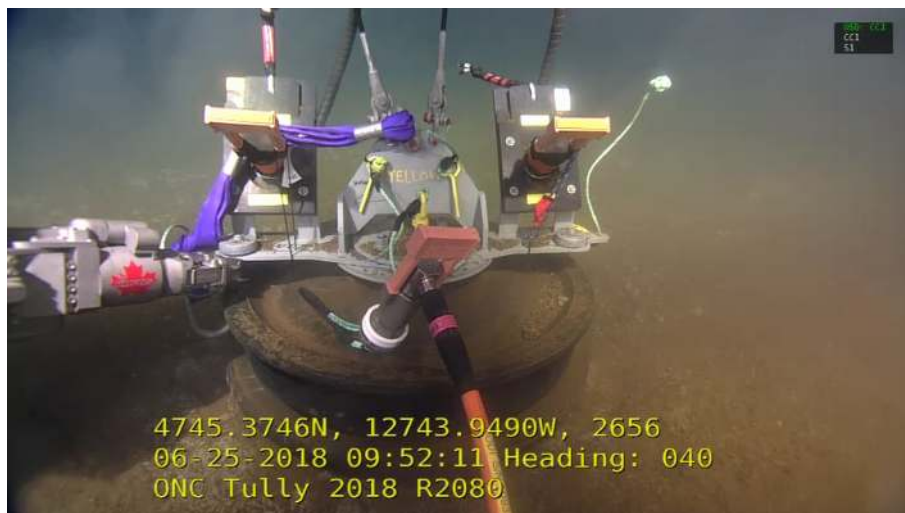


Figure 11.5: The ROV is rotating the anchor in such a way that the modules face each other. The orange ODI cable leads to the instrument platform and is connected afterwards.

---

# Conclusion

The STRAW project has shown that Ocean Networks Canada provides a suitable infrastructure for a larger future installation and invaluable help to sub-sea experiments, which made the development and deployment of two strings in less than eight months possible. The methods used in the string construction have proven to be viable, the POCAM calibration module has been further improved and a new detection module, the SDOM, has been developed. Additionally a convenient system for string deployments from ships has been developed and tested. If the data taken shows promising results, STRAW could be the first step towards a cubic kilometer detector in the Pacific Ocean, expanding, together with GVD and KM3Net on the Northern Hemisphere, and IceCube on the Southern hemisphere, our view to the full sky and giving new impulses to neutrino astronomy.

# Bibliography

- [Aab+15] Alexander Aab et al. “The Pierre Auger Cosmic Ray Observatory”. In: *Nucl. Instrum. Meth.* A798 (2015), pp. 172–213. doi: 10.1016/j.nima.2015.06.058. arXiv: 1502.01323 [astro-ph.IM].
- [Aar+13] M. G. Aartsen et al. “Probing the origin of cosmic rays with extremely high energy neutrinos using the IceCube Observatory”. In: *Phys. Rev.* D88 (2013), p. 112008. doi: 10.1103/PhysRevD.88.112008. arXiv: 1310.5477 [astro-ph.HE].
- [Aar+16] M. G. Aartsen et al. “Observation and Characterization of a Cosmic Muon Neutrino Flux from the Northern Hemisphere using six years of IceCube data”. In: *Astrophys. J.* 833.1 (2016), p. 3. doi: 10.3847/0004-637X/833/1/3. arXiv: 1607.08006 [astro-ph.HE].
- [Abb+13] R. Abbasi et al. “IceTop: The surface component of IceCube”. In: *Nucl. Instrum. Meth.* A700 (2013), pp. 188–220. doi: 10.1016/j.nima.2012.10.067. arXiv: 1207.6326 [astro-ph.IM].
- [ANT05] ANTARES Collaboration. “Transmission of light in deep sea water at the site of the Antares neutrino telescope”. In: *Astropart.Phys* 23 (2005), pp. 131–155. doi: 10.1016/j.astropartphys.2004.11.006.
- [Bel+14] G. Bellini et al. “Neutrinos from the primary proton–proton fusion process in the Sun”. In: *Nature* 512.7515 (2014), pp. 383–386. doi: 10.1038/nature13702.
- [BH98] Craig F. Bohren and Donald R. Huffman. *Absorption and scattering of light by small particles*. 2nd ed. Wiley, 1998. ISBN: 978-0-471-29340-8.
- [BOR10] E. Baur, T. A. Osswald, and N. Rudolph. *Saechtling Kunststoff Taschenbuch*. Hanser, 2010. ISBN: 978-3-446-43442-4.
- [Cap+02] A. Capone et al. “Measurements of light transmission in deep Sea with the AC9 transmissometer”. In: *Nucl.Instrum.Meth.* A487 (2002), pp. 423–434. doi: 10.1016/S0168-9002(01)02194-5.
- [Cle+98] B. T. Cleveland et al. “Measurement of the solar electron neutrino flux with the Homestake chlorine detector”. In: *Astrophys. J.* 496 (1998), pp. 505–526. doi: 10.1086/305343.
- [Coo70] Albert R. Cook. “The Role of Zinc in the Corrosion Protection of Offshore Structures”. In: *Jom* 22.4 (1970), pp. 40–45. doi: 10.1007/bf03355635.

- [Cow+56] C.L. Cowan et al. “Detection of the Free Neutrino: a Confirmation”. In: *The Theory of Beta-Decay* (1956), pp. 129–135. doi: 10.1016/b978-0-08-006509-0.50008-9.
- [Cyb+05] Richard H. Cyburt et al. “New BBN limits on physics beyond the standard model from  $^4\text{He}$ ”. In: *Astropart. Phys.* 23 (2005), pp. 313–323. doi: 10.1016/j.astropartphys.2005.01.005. arXiv: astro-ph/0408033 [astro-ph].
- [Dan+62] G. Danby et al. “Observation of high-energy neutrino reactions and the existence of two kinds of neutrinos”. In: *10.1103/PhysRevLett.9.36* (1962). doi: 10.1103/PhysRevLett.9.36.
- [DNV] *DNV-RP-B401: Cathodic Protection Design*. <https://rules.dnvgl.com/docs/pdf/DNV/codes/docs/2011-04/RP-B401.pdf>, accessed 07.10.18. Det Norske Veritas. Oct. 2010.
- [DUM] H. Bradner for the DUMAND Collaboration. *Attenuation of light in clear deep ocean water*. [http://www.inp.demokritos.gr/web2/nesstor/www/2nd/files/247\\_252\\_bradner.pdf](http://www.inp.demokritos.gr/web2/nesstor/www/2nd/files/247_252_bradner.pdf).
- [Fol+15] Brent Follin et al. “First Detection of the Acoustic Oscillation Phase Shift Expected from the Cosmic Neutrino Background”. In: *Phys. Rev. Lett.* 115.9 (2015), p. 091301. doi: 10.1103/PhysRevLett.115.091301. arXiv: 1503.07863 [astro-ph.CO].
- [Fra+87] G. S. Frankel et al. “Metastable Pitting of Stainless Steel”. In: *Corrosion* 43.7 (1987), pp. 429–436. doi: 10.5006/1.3583880.
- [Fuk15] Masaki Fukushima. “Recent Results from Telescope Array”. In: *EPJ Web Conf.* 99 (2015), p. 04004. doi: 10.1051/epjconf/20159904004. arXiv: 1503.06961 [astro-ph.HE].
- [Gär16] Andreas Gärtner. *Realization of the “Precision Optical Calibration Module” prototype for calibration of IceCube-Gen2*. BA thesis, [https://www.cosmic-particles.ph.tum.de/fileadmin/w00bk1/www/Thesis/gaertner\\_BA.pdf](https://www.cosmic-particles.ph.tum.de/fileadmin/w00bk1/www/Thesis/gaertner_BA.pdf). July 2016.
- [Hei+] Max Heinzler et al. *Tabellenbuch Metall*. 40th ed. Europa Lehrmittel. ISBN: 978-3-8085-1727-7.
- [Hen] *Image by F. Henningsen of ECP*.
- [Hen18] Felix Henningsen. “Optical Characterization of the Deep Pacific Ocean: Development of an Optical Sensor Array for a Future Neutrino Telescope”. MA thesis. Technical University of Munich, July 2018.
- [Hil18] Simon Hiller. “STRAW: Entwicklung der Hardware Komponenten”. MA thesis. Technical University of Munich, Aug. 2018.
- [Hir+87] K. Hirata et al. “Observation of a Neutrino Burst from the Supernova SN 1987a”. In: *Phys. Rev. Lett.* 58 (1987). [727(1987)], pp. 1490–1493. doi: 10.1103/PhysRevLett.58.1490.
- [HK08] F. Halzen and S. R. Klein. “Astronomy and astrophysics with neutrinos”. In: *Physics Today* 61, 5, 29 (2008), pp. 29–35. doi: {10.1063/1.2930733}.
- [Jan17] H. -Th. Janka. “Neutrino Emission from Supernovae”. In: (2017). doi: 10.1007/978-3-319-21846-5\_4. arXiv: 1702.08713 [astro-ph.HE].

- [Jer76] N.G. Jerlov. *Marine Optics*. Amsterdam: Elsevier, 1976. ISBN: 978-0-080-87050-2.
- [JOT10] “Was das Feuerverzinken wirklich kann”. In: *JOT Journal für Oberflächentechnik* 50.2 (2010), pp. 34–36. DOI: 10.1007/bf03252512.
- [Jur+16] M. Jurkovič et al. “A Precision Optical Calibration Module (POCAM) for IceCube-Gen2”. In: *EPJ Web Conf.* 116 (2016), p. 06001. DOI: 10.1051/epjconf/201611606001.
- [Kae79] Helmut Kaesche. *Die Korrosion der Metalle*. 1979. Chap. Lochfraßkorrosion. DOI: 10.1007/978-3-662-11502-2.
- [Kap+85] J.S. Kapustinsky et al. “A fast timing light pulser for scintillation detectors”. In: *Nuclear Instruments and Methods in Physics Research Section A: Accelerators, Spectrometers, Detectors and Associated Equipment* 241.2 (1985), pp. 612–613. ISSN: 0168-9002. DOI: 10.1016/0168-9002(85)90622-9. URL: <http://www.sciencedirect.com/science/article/pii/0168900285906229>.
- [Kod+01] K. Kodama et al. “Observation of tau neutrino interactions”. In: *Phys. Lett. B* 504 (2001), pp. 218–224. DOI: 10.1016/S0370-2693(01)00307-0. arXiv: hep-ex/0012035 [hep-ex].
- [KS16] M. Kok and T. B. Schön. “Magnetometer calibration using inertial sensors”. In: *IEEE Sensors Journal, Volume 16, Issue 14, Pages 5679–5689* (2016).
- [Leh70] Joseph A. Lehmann. “Cathodic Protection of Offshore Structures”. In: *Jom* 22.3 (1970), pp. 56–63. DOI: 10.1007/bf03355632.
- [LSN97] N.j. Laycock, J. Stewart, and R.c. Newman. “The initiation of crevice corrosion in stainless steels”. In: *Corrosion Science* 39.10-11 (1997), pp. 1791–1809. DOI: 10.1016/S0010-938X(97)00050-4.
- [LV06] B. K. Lubsandorzhev and Y. E. Vyatchin. “Studies of ‘Kapustinsky’s’ light pulser timing characteristics”. In: *JINST* 1,T06001 (2006).
- [McD05] A. B. McDonald. “Evidence for neutrino oscillations. I. Solar and reactor neutrinos”. In: *Nucl. Phys. A* 751 (2005), pp. 53–66. DOI: 10.1016/j.nuclphysa.2005.02.102. arXiv: nucl-ex/0412005 [nucl-ex].
- [Mie08] Gustav Mie. “Beiträge zur Optik trüber Medien, speziell kolloidaler Metallösungen”. In: *Annalen der Physik* 330.3 (1908), pp. 377–445. DOI: 10.1002/andp.19083300302.
- [Oli+14] K. A. Olive et al. “Review of Particle Physics”. In: *Chin. Phys. C* 38 (2014), p. 090001. DOI: 10.1088/1674-1137/38/9/090001.
- [ONC1] *Ocean Networks Canada Homepage*. <http://www.oceannetworks.ca/>. accessed: 28.10.2018.
- [ONC2] *Ocean Networks Canada Strategic Plan 2016-2021*. <http://www.oceannetworks.ca/sites/default/files/pdf/ONCStrategicPlan2016-2021.pdf>. accessed: 28.10.2018.
- [PDG18] M. Tanabashi et al. (Particle Data Group). “Review of Particle Physics”. In: *Phys. Rev. D* 98, 03001 (2018).

- [Pun04] C. Punckt. “Sudden Onset of Pitting Corrosion on Stainless Steel as a Critical Phenomenon”. In: *Science* 305.5687 (2004), pp. 1133–1136. doi: 10.1126/science.1101358.
- [SB81] R. C. Smith and K. S. Baker. “Optical properties of the clearest natural waters”. In: *Applied Optics* 20 (2 1981), pp. 177–184.
- [SB91] L. Stockert and H. Böhni. “Susceptibility to Crevice Corrosion and Metastable Pitting of Stainless Steels”. In: *Materials Science Forum* 44-45 (1991), pp. 313–328. doi: 10.4028/www.scientific.net/msf.44-45.313.
- [Spa17] Christian Spannfellner. *Realisierung des ersten Precision Optical Calibration Modules für das Gigaton Volume Detector Neutrino Teleskop in Baikal*. BA thesis, [https://www.cosmic-particles.ph.tum.de/fileadmin/w00bk1/www/Thesis/BA\\_Christian\\_Spannfellner.pdf](https://www.cosmic-particles.ph.tum.de/fileadmin/w00bk1/www/Thesis/BA_Christian_Spannfellner.pdf). July 2017.
- [Wil14] Dawn Williams. “Search for Ultra-High Energy Tau Neutrinos in IceCube”. In: *Nucl. Phys. Proc. Suppl.* 253-255 (2014), pp. 155–158. doi: 10.1016/j.nuclphysbps.2014.09.038.
- [WT87] P. P. E. Weaver and J. Thomson. *Geology and Geochemistry of Abyssal Plains*. London: Geological Society, 1987. ISBN: 978-0-632-01744-7.
- [Wür] Würth. *Dimensionierung von metrischen Schraubenverbindungen*. [https://www.wuerth-industrie.com/web/media/de/pictures/wuerthindustrie/technikportal/dinokapitel/Kapitel\\_06\\_DINO\\_techn\\_Teil.pdf](https://www.wuerth-industrie.com/web/media/de/pictures/wuerthindustrie/technikportal/dinokapitel/Kapitel_06_DINO_techn_Teil.pdf), retrieved on 10.10.18.
- [ZK66] G. T. Zatsepin and V. A. Kuzmin. “Upper limit of the spectrum of cosmic rays”. In: *JETP Lett.* 4 (1966). [Pisma Zh. Eksp. Teor. Fiz.4,114(1966)], pp. 78–80.